MULTIFUNCTIONAL COMPOSITES AND DEVICES FOR SENSING

AND ENERGY HARVESTING

A Thesis

by

MICHAEL ALLEN CLEVELAND

Submitted to the Office of Graduate Studies of
Texas A&M University
in partial fulfillment of the requirements for the degree of

MASTER OF SCIENCE

May 2010

Major Subject: Mechanical Engineering

MULTIFUNCTIONAL COMPOSITES AND DEVICES FOR SENSING

AND ENERGY HARVESTING

A Thesis

by

MICHAEL ALLEN CLEVELAND

Submitted to the Office of Graduate Studies of
Texas A&M University
in partial fulfillment of the requirements for the degree of

MASTER OF SCIENCE

Approved by:

Chair of Committee,	Hong Liang
Committee Members,	Dennis O'Neal
	Bradleigh Vinson
Head of Department,	Dennis O'Neal

May 2010

Major Subject: Mechanical Engineering

ABSTRACT

Multifunctional Composites and Devices for Sensing and Energy Harvesting.

(May 2010)

Michael Allen Cleveland, B.A., Austin College

Chair of Advisory Committee: Dr. Hong Liang

This research investigates a novel class of active materials for energy and sensing applications. Magnetocaloric alloys, $Gd_5Si_2Ge_2$, were developed into a composite with poly(vinylidine flouride) (PVDF), piezoelectric polymer. The giant megnetocaloric property combined with the piezoelectricity creates extraordinary properties for composite materials.

The research approach was primarily experimental. Activities include synthesis, characterization, and device design and evaluation. Using the arc melting method, the magenetocaloric samples were created. Multi-length scales characterized using atomic force microscopy (AFM), optical microscopy, scanning electron microscopy (SEM) with energy dispersive spectroscopy (EDS), X-Ray diffraction (XRD), and X-Ray Photoelectron spectroscopy (XPS). The prototype devices were evaluated for their power generation and efficiency. Through those techniques, the fundamental understanding in the new materials was obtained. The relationships between process-microstructures, microstructure-properties, and structure-power generation were established.

Results showed that the phase transformation of the magnetocaloric material at its Curie temperature induced a significant increase in power generation in the

peizeoelectric polymer. Such transition was also beneficial for a laminated device for energy harvesting. In addition, it was found that the oxidation that occurred during high temperature melting stabilized the orthorhombic phase at room temperature. The multifunctional composites as well as the laminated structure use the thermal expansion of the magnetocaloric material for energy harvesting, cyclic monitoring, and/or thermal switching.

This thesis consists of six chapters. Chapter I provides a history and explanation of the materials used. Chapter II provides an explanation of the motivation for this work. Chapter III addresses the experimental procedures. The results of which are presented in Chapter IV and discussed in Chapter V. The research is summarized and future recommendations are given in Chapter VI.

ACKNOWLEDGEMENTS

NOMENCLATURE

AFM   Atomic Force Microscopy

COP   Coefficient of Preformance

DMSO   Dimethyl Sulfoxide

EDS   Energy Dispersive X-Ray Spectroscopy

GSG $Gd_5(Si_xGe_{1-x})_4$ Family of Alloys

HCFC   Hydrochlorofluorocarbons

PTrFE   Poly(trifluoroethylene)

PVDF   Poly(vinylidene fluoride)

PZT   Lead Zirconate Titanate

SEM   Scanning Electron Microscopy

TrFE   Trifluoroethylene

XPS   X-Ray Photoelectron Spectroscopy

XRD   X-Ray Diffraction

TABLE OF CONTENTS

LIST OF FIGURES

LIST OF TABLES

CHAPTER I

INTRODUCTION

This chapter provides background information necessary to understand the subject of this research. The needs within the fields of energy harvesting and sensing applications are discussed. A discussion of the development of magnetocaloric materials and their applications in the field of magnetic refrigeration and progress made in that field is provided. The mechanism for the behavior of magnetocaloric materials is described. The history of piezoelectric polymers is then discussed including the development of PVDF and ends with an explanation of the behavior of PVDF.

1.1 Energy Needs and Mechanical-Electro-Power Generation

One of the biggest problems for the advancement of device technology is the ability to power them. Advancement in related technologies has grown at an exponential rate in the past several years.[1] This is particularly true in microelectronics, as its development has been predicted by Moore's law, i.e., in every eighteen months, the transistor density doubles.[2] The fast pace in growth has placed a unique strain on powering those devices. On the contrary, the growth of power density in batteries has grown only linearly.[1] This presents a major problem in the area of portable computing and implanted electronic devices.

As the ability for electronic sensing increases, wide applications will be created to implant sensing devices in remote or unreachable locations. For example, devices like vibration monitors implanted in walls do not have access to standard power sources.[3]

_____

This thesis follows the style of *Journal of Applied Physics*.

The most apparent feature of these sensors is the difficulty of access. If these devices could scavenge energy from its surroundings, they could function indefinitely. This situation is one of many that serves as the impetus of energy harvesting.

There have been a variety of studies on harvesting the mechanical energy from the surroundings, ranging from small to large scales. [4-6] Relatively few studies have been conducted that use thermal energy. Several studies have attempted thermoelectric energy harvesting but have been limited to specific scenarios and pure thermoelectric materials.[7-11]

Piezoelectric based methods are particularly appealing because of their versatility and small form factors. The majority of the work thus far has focused on piezoceramics, like Lead Zirconate Titanate (PZT), because of the higher piezoelectric response.[12] There are certain applications favoring low cost, flexible, piezoelectric polymers for energy harvesting. For example, Ocean Power Technologies have produced an energy-harvesting eel that uses the flow of water in a river or ocean to produce an oscillating motion that is converted into power by piezoelectric polymers.[13] It has also been shown that small sections (5.62mm radius) of poly(vinylidene fluoride) (PVDF) compressed at 1 Hz frequencies can produce power levels of .33 uW, which is enough to power small Bio-MEMS devices for monitoring the human body.[12] Micro-electro-mechanical systems, developed for specific applications, are coming of age as manufacturable systems.[14-16]

PVDF is a piezoelectric polymer. Under mechanical motion, it can generate electrical potential. Recent studies has shown that, during power generation, the material undergoes phase transformation.[17] PVDF is particularly attractive for dynamic

applications. The most common application of PVDF is its use in coaxial cables as a shielding material. It is possible to make coaxial cables with poled PVDF so that they are piezoelectric, allowing the cable to serve dual purposes.[18] Another advantage of PVDF is its high chemical resistance, which makes it appealing for harsh environments.

1.2 Magnetocaloric Materials

1.2.1   History of Magnetocaloric Effect

The magnetocaloric effect is the property of certain materials to change their heat capacity under applied magnetic fields. Since its discovery in 1880, the magnetocaloric effect has been studied in a variety of metals under different conditions. Many fields could be revolutionized by this property, particularly that of refrigeration. The first use of this property for cooling purpose was by the Nobel Laureate William F. Giauque and his colleagues. They used $Gd_2(SO_4)_2*8H_2O$ as a coolant material by demagnetization of the material with a 8,000 Gauss iron cored electromagnet.[19] This work proved the viability of this property for cooling purposes. Giauque's work laid the foundation for the current effort on the development of magnetocaloric refrigerators.

The current state of the magnetocaloric refrigerators is in the development of proof-of-concept systems and further optimization. Also, there is need in the development of particular sensing mechanisms for cyclic monitoring systems and additional microstructure studies. Certain magnetocaloric materials have the ability to serve as an active component in sensing materials and devices.

1.2.1.1 Discovery of Giant Magnetocaloric Materials

Work funded by the Advanced Energy Projects led to significant advancements in the materials used in magnetic cooling devices. In 1997, Pecharsky and Gschneidner discovered that $Gd_5Si_2Ge_2$ is able to produce a 50% larger magnetocaloric effect than that of pure Gd metal with a Curie temperature 25 Kelvin, lower than Gd metal.[20] This effect is due to the magnetic phase transformation at 270 Kelvin.[21] By decreasing the amount of Si and Ge in the system and replacing it with small amounts of Ga, the transition temperature could be increased up to 285 Kelvin without any significant loss in the magnetocaloric effects.[22] In addition, the transition temperature could be tailored from 40 K to the original 270 K by varying the Si and Ge rations.[23] Also, it was possible to reduce the magnetocaloric effect, and increase the transition temperature (Curie temperature) up to 335K by increasing the Si concentration to above 50%..[23]

Since the discovery of $Gd_5Si_2Ge_2$ (GSG), there have been a variety of studies on the effects of various conditions on the behavior of GSG. In 2006, Basso studied the effects of melting on the thermodynamics of these materials and mapped the thermodynamic transitions.[24] Other studies sought to explain the structure of this material using a variety of experimental techniques, from XRD to photoelectron spectroscopy.[25,26] The most important contribution to this report was finding the existence of the large thermal expansion (or contraction) accompanying the transition at the Curie point. This fact was first considered by Han et al. in 2002.[27] He studied the effects of purity on the thermal expansion, as well as the thermal expansion of single crystals.[28,29] The influence of O, Fe, Ga and Mn on $Gd_5Si_2Ge_2$'s structure and thermodynamics during phase transformations have been reported.[21-47]

The discovery of GSG led to the discovery of several other materials in the same family. These discoveries include $Tb_5Si_2Ge_2$, MnAs, $MnAs_{1-x}Sb_x$, and La $(Fe_{1-x}Si_x)_{13}$, as well as the family of materials like $MnFeP_{0.45}As_{0.55}$ and the related $MnFeP_xAs_{1-x}$ alloys.[48,49].

The $La(Fe_{1-x}Si_x)_{13}$ alloys are particularly appealing because the majority of the material is made of low cost and readily available materials.[50] One of the critical factors for producing magnetocaloric materials is purity, since concentrations of a few parts per million can produce noticeably negative impacts on the performance of the material.[28] The $La(Fe_{1-x}Si_x)_{13}$ alloys are made of materials that exist in high purity commercially. Unlike the GSG material, they do not have a structural change that accompanies their magnetic ordering, making them appealing from a design standpoint since the thermal expansion does not have to be accounted for. However, their Curie temperature ranges from 200 to 263 Kelvin, making them less than ideal for high temperature applications. Additionally, since traditional arc melting processes do not reliably produce single-phase samples, melt spinning and annealing must be done to ensure that the materials are in the correct phase.[50,51]

The MnAs based compounds are interesting because of the low cost of the materials but present a problem for processing and maintenance of the systems due to their poisonous nature. Since the Mn is covalently bonded to the As, it should be environmentally stable, but this has yet to be experimentally verified. The Curie temperature for these materials is around 307 K making it ideal for room temperature based magnetic refrigeration.[52]

The Heusler alloys, which contain Ni_2MnGa, also exhibit strong magnetocaloric properties. They undergo a temperature induced martensitic transition. The alloy, Ni_2MnGa, was found to order ferromagneticly at 376 Kelvin. It has a magnetic moment of 4.17 uB, mostly due to the Mn atoms and a small amount being confined to the Ni atoms.[55] The material also has a martensitic transformation at 220 Kelvin that can be increased to room temperature by varying the concentration of the elements. This transformation has a large anisotropy and it is accompanied by a large strain due to the crystal phase change. The deformation is 6.5% in the (001) crystal direction and is difficult to compensate for in the design refrigeration applications. In order to be effective, the material must be a single crystal, which is costly to produce in commercial quantities. Strain in the polycrystalline samples will cause the samples to severely crack after a few cycles making them incapable of use in magnetic refrigerators.[56]

Certain Fe_2P based alloys are of particular interest, as well, because they can be easily produced and have near room temperature Curie temperatures. The most popular of which is the MnFe(P,As) alloys. Fabrication involves ball-milling chips of Fe_2P or $FeAs_2$, Mn and P powder. The amorphous powder is pressed into shape and then heated in an Argon filled Quartz tube at 1273 for an hour followed by a homogenization process. The magnetocaloric effect produced by these materials is significant and doesn't have volume expansion problems like the Heusler or GSG alloys.[51] To summarize the materials discussed above, Table 1 provides a list of these materials list.

Table 1 Comparison of existing magnetocaloric materials.

Material	Temperature Range (K)	delta T (under 2T)	Reference
Gd	270-310	5.8	[53]
GSG	150-290	6.6	[20,41]
La(Fe,Si)H	180-320	7	[54]
MnAs	220-320	4.1	[52]
MnNiGa	310-350	2	[47]
MnFe(P,As)	150-450	6	[51]

While these materials are readily available and exhibit strong magnetic properties, it does not make them suitable for magnetic refrigeration. There are three requirements for these materials to be strong candidates for magnetic refrigerants. First, the material should exhibit a large entropy change due to magnetic transformations. Most of these materials have a large structural entropy change, as well as a large magnetic entropy change. The structural change should be coupled with the magnetic entropy change to achieve the optimum results. GSG is one of the few materials with a coupled magnetic and structural change. Second, the material should have a large adiabatic temperature change to maximize its ability as a refrigerant material. Third, the material should have strong mechanical properties. There have been problems with the stability of GSG because it degrades into a powder. This doesn't negatively impact the magnetic

properties, but does present a design problem. The GSG has been composited into other metals for structural applications. [55]

1.2.2   Function of GSG

GSG exhibits the giant magnetocaloric effect, which corresponds to a change in heat capacity depending on the applied magnetic field and temperature. [18] This phenomenon occurs because of the particular crystal structures and phase changes. The magnetic considerations of this material can be suspended in this work for simplicity and be focused on the zero applied magnetic field transition that occurs at -4 degrees Celsius. This phase transformation is from the orthorhombic phase to the monoclinic, which are two crystal structures that have different heat capacities as noted by Pecharsky.[20] A volume change, caused by the phase transformation, accounts for the large thermal expansion of the material described by Han et al.[26] The lattice parameters for each structure in Table 1, as well as their volumes and the percent difference.

Table 2 Table of lattice parameters for GSG alloys.[25]

	Monoclinic	Orthorhombic	% Change
a (Å)	7.585	7.443919	-1.86
b (Å)	14.8	14.81036	0.07
c (Å)	7.777	7.8259951	0.63
β	93.29		
Volume(Å3)	871.5915793	862.7934225	1.009435729

1.2.2.1 High Temperature Phase Transformation

Synthesis of this material depends on the high temperature phase changes and should be considered when tailoring the processing conditions to this material. There was one report about high temperature phase transformation of GSG discovered by Mozharivskyj et al. [36] Their study indicated that the monoclinic to orthorhombic phase transformation was reversible under slow cooling and heating at high temperatures. However, it was not reversible under rapid cooling, meaning that the crystal phase structure was locked in the place and not entirely stable. The presence of oxygen and nitrogen impurities was found to stabilize the orthorhombic phase below 300 degrees Celsius. [45] As such, the monoclinic phase above this temperature became stable. These impurities caused the orthorhombic to monoclinic phase transformation to be irreversible, severely limiting the magnetocaloric properties of the materials.[46]

As discussed, if a process undergoes rapid cooling, an irreversible monoclinic phase is expected to remain. The high temperature phase, trapped at low temperatures, is meta-stable. It is expected that this phase will spontaneously decompose and cause cracking of the material. [38]

1.2.3   Conceptual of Magnetic Refrigeration

The unique properties of magnetocaloric materials enable them to make effective refrigerators. This is possible because the materials contain two coupled energy storage mechanisms. In most other materials, phonon excitations give rise to their temperature. In magnetocaloric materials, however, the phonon excitations are coupled to the spin of

the electrons. Under an applied magnetic field, the aligned magnetic dipoles of the material align the lattice as well. [57]

A refrigerator can use the coupled properties of these materials by subjecting them to an ordered cycle of conditions. The first stage involves randomly ordered magnetic moments, then a magnetic field is applied to align the moments. This results in the heating of the material. The heat is then dissipated to the surroundings by thermal transfer. When the magnetic field is removed, the material cools resulting in heat from the load being transferred to the magnetic refrigerant. This cycle is repeated until the desired temperature, or the limit of the system, is reached. The larger the change in temperature produced by the material, the better refrigerating system. This is what makes the giant magnetocaloric effect materials appealing.

The advantages of magnetic refrigerators are numerous and will become apparent as the limits of gas cycle refrigerators are approached. The most apparent advantage is the reduction of the use of complex or environmentally damaging substances, like HCFCs and ammonia. Additionally, the lack of expanding gasses and large compressors reduces the noise and size of the refrigeration system. Some designs of magnetic refrigerators have no moving parts; meaning that the noise, size and maintenance times can all be greatly improved. [57] Most importantly, it has been found that magnetic refrigerators can be 30% more efficient than their gas counterparts if magnetic fields larger than 5 T can be used. [58]

1.2.3.1 Early Low Temperature Magnetic Cooling Systems

Cyclic magnetic refrigeration was first reported in 1954 when Collins and Zimmerman published their work on continuously operating refrigerators. This apparatus operated at both 1 and 0.73 Kelvin and functioned by magnetizing and demagnetizing iron ammonium alum periodically.[56] In 1955, Heer et al. produced an apparatus that operated at 0.2 Kelvin. [59] This particular apparatus was able to extract 123 erg/s (12.3 uJ/s) from the cold reservoir with an operating frequency of 1/120 Hz. In both of these systems, liquid helium was used as an initial coolant, so the change in temperature was not more than 3 Kelvin. While these apparatuses were successful in low temperature work, their performance pales in comparison to that of the modern high temperature work.

1.2.3.2 High Temperature Study

In 1976, Brown proposed that it was possible to create a temperature difference larger than that of the adiabatic temperature change using a reciprocating magnetic refrigerator. [60] This established a basis using magnetocaloric materials for high temperature applications. In his approach, Brown was able to achieve a temperature difference of 47 Kelvin and eventually achieved a temperature difference of 80 Kelvin. [60]

Several studies were conducted by various groups in the magnetocaloric-cooling principal in comparison to different cycles. [61] Chen and Yan concluded that, near room temperature, regenerative magnetic refrigerators were more efficient than Carnot, Ericsson or Stirling cycles. [62-64]

The field was revolutionized when Gschneidner and Barclay started working on new materials for use in magnetic cooling systems. In 1991, the Astronautics Corporation of America contracted the Ames Laboratory to develop a new material to be used in low temperature cooling for the liquefaction of hydrogen gas. It was desired to replace GdPd because of the high cost of Pd. The product of this research was $(Dy_{0.5}Er_{0.5})Al_2$.[65] This material successfully replaced GdPd with inexpensive Al. Dy and Er were only marginally more expensive than Gd. This work led to a long term cooperative research and development agreement, which tested prototype materials for industrial applications. [58]

In addition to new materials, cost analysis done by the Ames Lab. found that a magnetic refrigerator could be 30% more efficient than a traditional gas cycle refrigerator and could offset the cost difference in 5 years in a large-scale system. Moreover, it would eliminate the environmental concerns of ammonia or other substances in a gas refrigerator. This led the Ames lab. to develop a high temperature demonstration unit with the funds from the Department of Energy.[58]

This demonstration unit used Gd metal as the refrigerant and ran for 5,000 hours over the course of 18 months without incident. It was designed to compete with large scale building air conditioners or freezers. It achieved a cooling power of 600 W, and a 60% Carnot efficiency with a 10-Kelvin temperature span with the use of a 50 kOe superconducting magnet with a coefficient of performance (COP) nearing 10.[57] It should be noted that until this point no magnetic refrigeration unit had run longer than a few hours or functioned on this scale. It was a powerful motivator in the field of magnetic cooling and is remarkable that the first major attempt was so successful.

After the success of the first generation magnetic refrigerator, a second-generation machine that allowed for greater cooling power and more variability was made. It was found in the first generation that a cycle time of 6 seconds is insufficient for a practical magnetic refrigerator since higher frequencies perform better. Additionally, it was desired to use a permanent magnet because of practical problems with cooling the superconducting magnets. The end result was a refrigeration unit that used Gd, Ed and Er spheres in a rotating bed with a 15 kOe permanent magnet. This machine was able to produce 25 Kelvin temperature span. It ran for a total of 1500 hours from 2001 to 2007 and served as a valuable testing platform for the development of the third generation of magnetic cooling apparatus. It also showed the viability of simple mechanical designs for magnetic cooling.[56]

The third generation of magnetic cooling apparatuses aimed to produce a high efficiency air conditioner based on newer inter-metallic compounds. This system used two 15 kOe modified Halbach magnets that rotate while the magnetocaloric cooling material remains fixed. This design has significant advantages over previous systems because is greatly simplifies the design of the cooling fluid flow around the magnetic cooling material. Early testing showed that it was capable of producing 140 W of cooling and a 4 Kelvin temperature span.

Until this point, the discussion of magnetic refrigerators had been limited to the work conducted at the Ames Lab. After Zimm et al. published their work with the first generation of magnetic refrigerators, it produced a great deal of interest in the development of other magnetic cooling systems.[57] From 1998 to 2007, there have been

at least 25 different magnetic cooling systems built in laboratories around the world. This section will highlight a few of these and their respective capabilities.

 In 2000, Bohigas et al. was able to create a temperature difference of 5 Kelvin using permanent magnets producing only 5 kOe with olive oil as the heat transfer medium.[58] This system is relatively inexpensive, while still producing promising results. In 2002, Blumenfeld et al. produced a system that had no moving parts, and used a charging and discharging super conducting magnetic coil to produce the magnetic field. It does, however, have a long cycle time of 30 seconds.[59] This system was able to produce a temperature difference of 15 Kelvin in a 17 kOe magnetic field.

He et al. and Lu et al. were able to produce the first reciprocating apparatus using two 14 kOe permanent magnets. This device produced a cooling power of 40 W using 1 kg of refrigerant material; a no load temperature span of 25 Kelvin in 20 minutes.[60,61] The ability to use both Gd and GSG powders, which exhibit a higher magnetocaloric effect, is particularly appealing. The operation of this machine was only marginally improved using the GSG compound, indicating that there is room for optimization of the system.

Tura and Rowe, in 2007, were able to produce a compact rotary magnetic refrigerator using two pairs of concentric Halbach arrays set up. With the pairs, as one magnet was charging, the other was being demagnetized. This system used a stationary magnetocaloric bed that allowed for much simpler fluid flows around the cooling material.[56] The compact design and simple mechanics of this system made it promising for commercialization. It was able to produce a no load temperature difference of 15 K.

A variety of other systems have been produced that follow the basic format of the systems discussed here. Unfortunately these systems are still in their early phases and direct comparison to traditional gas refrigerators because the COP is not typically presented. The number of papers being published on magnetic cooling is growing at an exponential rate and is expected to reach a commercial level within the next few years, if the current trend continues. [62]

1.3 Poly(vinylidene fluoride)

This section will describe the history and development of piezoelectric polymers and some of their uses. The piezoelectric material has been widely commercialized for a wide variety of applications. This section will describe the physics that allow these materials to function and some of their resultant properties.

1.3.1.1 A Brief History of Piezoelectric Polymers

Piezoelectric polymers were first studied in 1925 when Eguchi investigated the electrets of carnauba wax and resin. [59] At elevated temperatures, the material maintained a charge in response to an applied electric field. [63] Piezopolymers weren't recognized or developed until the 1950's when Fukada conducted studies on the shear piezoelectricity of various biopolymers, such as cellulose, collagen and keratin. [ref.] Despite the low piezoelectric response of these materials, Fukada was able to make a gramophone pickup using piezoelectricity from tendon, bone and baleen.[64] In 1968, it was discovered that polymethyl-l-glutamate exhibited a shear piezoelectric constant of $d_{14} = -2$ pC/N. It was later used to make the electromechanical transducer of a microphone. [64] In the following year, it was discovered that poled polyvinylidene fluoride (PVDF) exhibited strong piezoelectric properties.[65]This discovery created a

great deal of work in polymer piezoelectrics, and is by far the most popular polymer piezoelectric material.[64] The complexity of polymers prevents a strong physical model from being developed to explain their properties. There are two main theories explaining the behavior of PVDF; the dimensional effect and intrinsic effect. [64] The dimensional effect states that the dipoles are pressed into the surface of the material under an applied stress. The intrinsic effect states that the applied stress causes the polarization of the dipoles, which induces the piezoelectric effect. Neither effect has been proven definitely dominant, but it is expected both mechanisms are present in the material. This topic will be discussed in more detail in later sections.

In 1974, Tamura et. al. discovered the dielectric hysteresis of PVDF. [65] In this study, the ionic conductivity was neglected by performing polarization experiments at -50 degrees Celsius. An applied electric field up to 240 MV/m produced a residual polarization of 60 mC/m^2. This study was expanded for a variety of temperatures, which provided the basic knowledge of the function of this material.[66]

Soon after the discovery of PVDF, it was found that many amorphous polymers exhibited the piezoelectric property as well. In 1980, Miyata et al. discoverd piezoelectricity in a copolymer of vinylidene cyanide and vinyl acetate. [67] A film of this copolymer was poled at 150 degrees Celsius near its glass transition temperature of 170 degrees Celsius, which caused a piezoelectric constant of d_{31} = ~5 pC/N. In 1984, Mathur et al. reported the hysteresis effects in the piezoelectric constants of odd numbered nylons. [67] While the piezoelectric constants were relatively weak for these materials, the fact that a whole class of polymers could exhibit the piezoelectric effect was particularly promising.

Of particular note is the fabrication of "single crystal" PVDF/TrFE films. These are highly crystalline thin films, instead of being a complete single crystal structure. All polymers contained some fraction of amorphous region, but these particular films had a very small amount of amorphous region and a nearly continuous crystalline section. In 1995, Ohigashi et al. published their work in producing the first single crystal thin films of PVDF. [68] The process of production was complicated and sensitive. Firstly, the solution of 75 molar% PVDF and 25 molar% PTrFE was film cast and drawn to 5 times its original length to orient the chains. Then, the film was clamped and supported only at the ends while it was annealed and crystallized for 2 hours at 138 degrees Celsius. After that, the film was poled by a 0.5 Hz AC field at room temperature. The properties of these films were improved over the standard "polycrystalline" PVDF/TrFE films.

1.3.1.2 PVDF Piezoelectric Function

To grasp the nature of PVDF's unique features, an understanding of polymer physical behavior should be firstly obtained. Polymers are long chain molecules that are composed of a single repeating unit called a "mer." The physical length varies greatly depending on the conditions, temperature, solvents, humidity etc. Consequently, the most useful parameter to describe the size of the polymer chains is the average molecular weight. Polymers can be compared for conceptual purposes to a bundle of threads or spaghetti noodles. When there is no apparent long range or local order, they are considered to be amorphous. In certain cases the polymer chains will fold and form small crystals to minimize their energy. This folding mechanism is an area of a great deal of research and the exact kinetics of its behavior is still being studied. The basic

shape of the crystal folding is accepted as similar to Figure 1. An amorphous region in most polymers surrounds these crystals.

Crystal plate
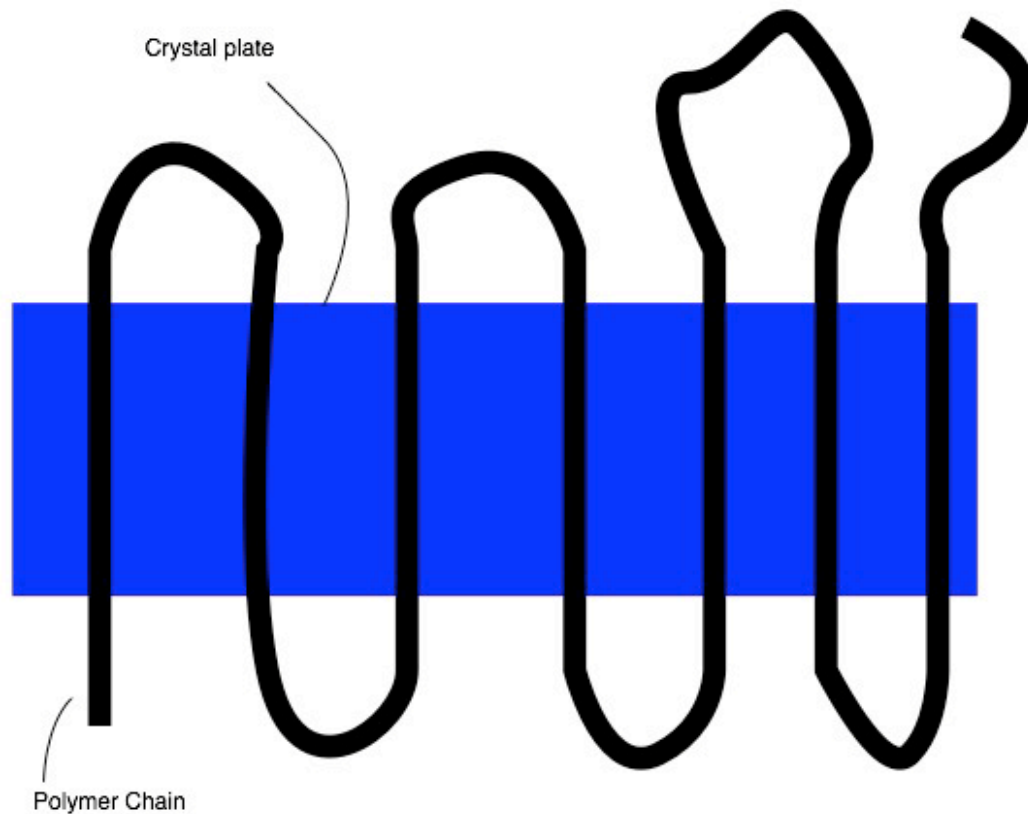
Polymer Chain

Figure 1 Polymer chain folding.

This chain folding is crucial for the behavior of PVDF. The structure of PVDF contains two large fluorine groups attached to a carbon atom as shown in Figure 2. This crystalline form gives PVDF its unique properties.
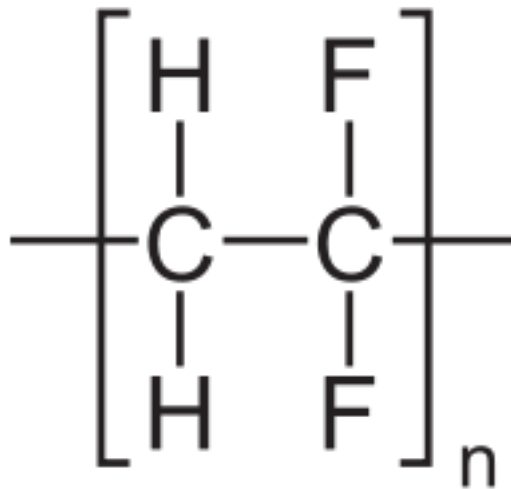
Figure 2 PVDF Monomer Unit.

The PVDF has four basic crystal types, labeled as alpha, beta, gamma, and delta. Each one of these crystals exhibits the piezoelectric effect to some degree, but the gamma phase exhibits the strongest response.

At least three of these modes are polar and exhibit the piezoelectric effect, with the delta phase most commonly associated with the piezoelectric effect in PVDF. The most common mode of PVDF is the alpha mode; this phase is not polar and not used as a sensor or actuator. This phase is most prevalent upon casting and typically accounts for 50-60 percent of the material, depending on the heating history. Upon application of a high electric field, usually on the order of 500 MV/m, the beta phase transitions into the delta phase. This electric field causes the chains to rotate and align, causing the polymer to exhibit the piezoelectric effect.

There are two major factors that cause polymers to exhibit the piezoelectric effect. Firstly, since the chains are polarized, an applied stress changes the orientation

and causes an electric field to be induced, which is based more heavily on electrostriction effects. This effect was best described by Wang et al. where it was found that a delta to beta phase transformation, caused the piezoelectric response in PVDF.[17] Secondly, the lateral applied stresses reduce the thickness of the film, which increases the induced charge on the electrodes; this effect is more mechanically based. [66] Piezoelectricity is quantified by four constants, which are illustrated in the Figure 3; These constants can be measured experimentally or modeled mathematically in a variety of ways.

$$d_{ij} = \left(\frac{\partial D_i}{\partial T_j}\right)^E = \left(\frac{\partial S_i}{\partial E_j}\right)^T$$

$$e_{ij} = \left(\frac{\partial D_i}{\partial S_j}\right)^E = -\left(\frac{\partial T_i}{\partial E_j}\right)^S$$

$$g_{ij} = -\left(\frac{\partial E_i}{\partial T_j}\right)^D = \left(\frac{\partial S_i}{\partial D_j}\right)^T$$

$$h_{ij} = \left(\frac{\partial E_i}{\partial S_j}\right)^E = -\left(\frac{\partial T_i}{\partial D_j}\right)^T$$

Figure 3 Piezoelectric constants.

Under an applied stress or strain, the generated electric field is given by the piezoelectric constant. However, if an applied electric field is present, then the reverse effect is possible, inducing a strain. This is called the converse piezoelectric effect. The

direct piezoelectric effect is given by the terms on the left in the equations above, while the converse effect is given by the terms on the right.

For PVDF, the largest constant is typically the d_{31} direction and the (11) direction is typically considered the poling direction. As a result, the largest piezoelectric effect comes about when the stress is applied normal to a plane perpendicular to the poling direction. The piezoelectric constants for PVDF are shown in Table 2.

Table 3 Table showing the typical piezoelectric constants of PVDF.[69]

d_{31} (pm/V)	g_{33} (mV-m/N)	k_{31}
28	240	0.12

This is the basic mechanism for the functioning of PVDF. In PVDF, the properties result from its crystal structures, which allows it to produce a strong electric field, inducing a current when applied to an electrode. This understanding of this material is crucial for the development of this research.

This chapter discussed about two actives materials, magnetocaloric alloys and piezoelectric polymers. The needs in alternative energy require novel materials. The present research focuses on development of new materials that will be discussed in following chapters.

CHAPTER II

MOTIVATIONS AND OBJECTIVES

As expressed in the last chapter there is little information available on the microstructure of as-cast GSG alloys. These alloys have great potentials to be used as magnetic refrigerants, high performance sensors, and energy harvesting. Thorough understanding of such a material needs to be obtained. Specifically, detailed study in processing-microstructure as well as performance will be investigated. The research will focus on GSG alloys, the synthesis processes, characterization, properties, and performance in terms of power generation. The objectives are as follows.

- Develop a process to synthesize magnetocaloric and piezoelectric polymer composites.

- Conduct multi-scale resolution characterization and spectroscopic analysis to obtain information of crystal and microstructures, morphology, chemical compositions, among others.

- Study the microstructure of as-cast GSG alloys through both chemical and structural techniques. Obtain fundamental understanding of the process-microstructure relationships.

- Develop multifunctional piezoelectric composites to serve as a sensing element and energy harvester. Develop a device to monitor the phase transformation of magnetocaloric refrigerants.

- Conduct energy analysis of developed materials and devices and estimate their efficiencies.

The primary research uses experimental approaches. It consists three major steps, synthesis, characterization, and device development.

During synthesis, an arc melting method will be used to generate the GSG materials. Independent process parameters are the sample size, arc current, number of melt cycles and melting time. These parameters will be used for optimization of the fabrication process. The characterization techniques include optical microscopy, scanning electron microscopy with energy dispersive X-ray spectroscopy, X-ray photoelectron spectroscopy and atomic force microscopy.

The performance evaluation focuses on the power generation by the composite and the device. The evaluation process will pass the systems through their Curie temperature and measure their piezoelectric response under the transition.

Device design is based on the consideration of key factors affecting the final outcome. Four designs will be carried out and each will be evaluated through their ability to function under the desired conditions for a large number of cycles as well as their power production.

This research has significant impacts on energy and sensing applications. Energy harvesting using piezoelectric materials has been rapidly developing but has been limited to novel applications of existing materials and has not developed new piezoelectric materials for harvesting energy from specific environments. An energy harvesting mechanism that focuses on the themomagnetic transition common in magnetic refrigerators and other situations should be developed to power auxiliary systems of these devices. Sensing elements are needed in magnetic refrigerators that would allow researchers to measure the lifetime and performance of the refrigerants. This means that

a cyclic monitoring system should be developed that measures the materials explicitly. Additionally, a thermal switch should be developed that allows other monitoring or notification systems to come online when the magnetocaloric refrigerants start their phase.

CHAPTER III

EXPERIMENTAL

This section describes the experimental procedure utilized in the research. It covers the properties of materials used, methods for the manufacture of the devices. Finally it will describe the characterization that was preformed on these materials.

Material preparation will be the first to be described since it is crucial for the characterization of the materials. This section will describe how the GSG material is cast and how the piezoelectric polymer devices and composites are formed.

Material characterization will be described by the different analytic techniques that were used. Additionally, the procedure for the operation of these machines will be briefly outlined here.

The order of the procedure follows the investigation of the properties. All relevant and technical procedures will be described in theory and in practice. Most steps will be better preformed if the user knows the exact mechanisms behind the procedure.

The theoretical discussion described in this section will explain the basic mechanisms behind the techniques. The description will highlight some of the advantages and limitations. This description will not be given if the process is readily apparent, as with optical microscopy.

3.1.   Materials

The aim of this research is to synthesize and characterize a novel class of new materials that uses GSG as its functional element. For the formation of GSG, pure Gd, Si

and Ge must be used. The properties of these materials greatly impact the production of

GSG. The important properties of these elements are shown in the table below.

Table 4 Table of properties for elements used in this research.

Name	Silicon	Germanium	Gadolinium
Abbreviation	Si	Ge	Gd
Atomic Number	14	32	64
Atomic Weight (g/mol)	28.0855	72.64	157.25
Melting Point (K)	1687	1211.4	1585
Density (kg m-3)	2330	5323	7901
Young's Modulus (GPa)	47		55
Thermal Conductivity (W m-1 K-1)	150	60	11
Commercial Purity	99.9999	99.999	99.9
Weight Percent in $Gd_5Si_2Ge_2$	5.7	14.7	79.6

From a processing standpoint, the most important features are melting point and

thermal conductivity. The highest melting point should be sufficiently exceeded so that

all materials are completely liquidities when being processed. The length of time for

processing should be long enough that the heat is transferred and distributed uniformly

in the material. This means that the highest thermally conductive materials must be

broken into small pieces and heated long enough to provide complete heat transfer. All of these considerations have been made in the process described in this section.

3.1.1. Arc Melting

3.1.1.1. Arc Melting Process

The theory behind arc melting is the exact same as that of arc welding but the conditions are changed to facilitate the manufacture of an ingot instead of a welded product. In both arc melting and arc welding an extremely high voltage is produced by a power supply. This voltage causes an electron arc to travel between the gap of the two electrodes and melts materials through heating. In typical arc melting furnaces the conditions are controlled to eliminate problems with contamination. The schematic of this setup is shown in Figure 4. In this Figure the tungsten electrode serves as the negative electron source in the process and is connected to the power supply. The sample is placed in the copper crucible, which serves as both the ground and the container for the liquid as it is being cast. All of these elements are enclosed in a vacuum chamber, which is not shown here for clarity.

Commercial purity elements were purchased from ESPI Metals Inc. Si and Ge in 99.9999% and 99.999% purity respectively while Gd was purchased in 99.9% purity. These purities are consistent or superior to previously published studies on this material.[20,21,27-29,40,41] The pure elements were then measured into their stociometric amounts by their mass to form $Gd_5Si_2Ge_2$. Once measured into their correct amounts they were mixed into a holding container and agitated by hand so that the powders and pieces were mixed before melting.

The samples were arc melted in a custom-built arc-melting furnace. The furnace has the capability for water-cooling and an argon environment. The chamber was evacuated by a vacuum pump to -30 psi and then filled with argon twice back to atmospheric pressure to ensure that the chamber had a minimal amount of gases that was combustible and prone to causing defects. The samples were then heated by the arc from a tungsten electrode through a water-cooled copper crucible in a circular pattern for 30 to 45 seconds to ensure complete melting of the sample. The sample was then removed and flipped over and re-melted to ensure proper mixing of the constituent materials. This process is repeated a total of four times to ensure that the samples are well mixed. Re-melting allows for elements that collect at the bottom of the sample to be moved and diffuse evenly through the sample.

Tungsten Electrode

Arc

Sample

Copper Crucible
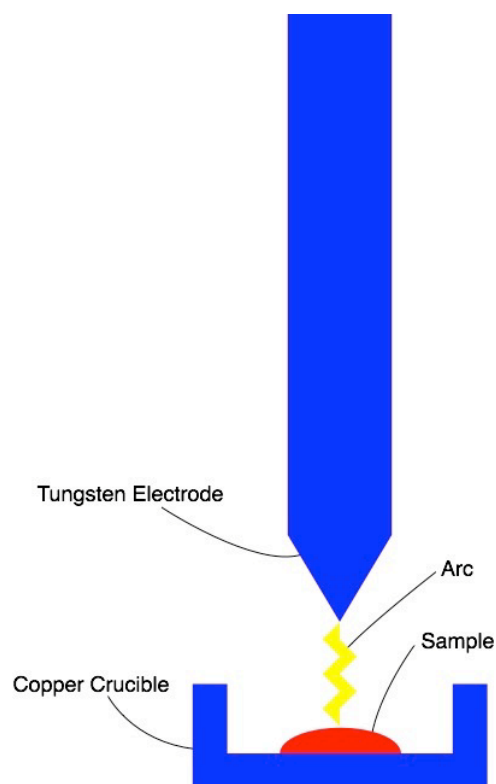
Figure 4 Diagram of the arc-melting furnace. Current is passed from the electrode through the sample to the crucible resulting in a visible arc.

3.1.1.2. Sample Heating Considerations

Trial and error with early samples ensured that the heating patterned liquefied the entire sample. It was found that with large, 20 gram, samples the low thermal conductivity of the sample prevented the areas not being directly exposed to the heat to solidify when they were expected to be liquid. This caused the sample to crack quite severely as it cooled making the samples unusable for anything but powder form. To remedy this problem samples were made 5g instead of 20g to help with the thermal

conductivity. This change greatly reduced the immediate cracking of the samples but the samples developed small cracks over time.

To address these small cracks, the heating pattern had to be changed to allow for a more consistent heating of both the top and bottom of the sample, this change in heating pattern is shown in Figure 5. This Figure shows the sample, depicted by the red area, and the path of the tungsten electrode and therefore the electron arc, depicted by the black curved line. Initially the arc was only moved above the sample only heating the top surface of the material.
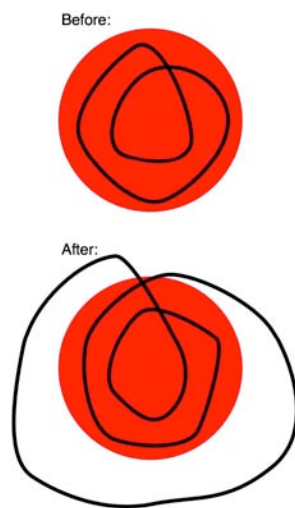
Figure 5 Diagram showing the change in the heating pattern. Note how the current method heats the sample and the crucible.

As can be seen in the diagram above, not only the sample top is heated but also the copper crucible surrounding the sample is heated in such a way that the heat is conducted through the copper and into the bottom of the sample. This causes the

temperature difference between the top and the bottom of the sample to be mitigated which reduces the cracking in the sample but does not completely eliminate the problem.

The cracking is partially caused by the heating difference and partially caused by the rapid cooling of the sample by the water-cooled crucible. To limit this effect the valves that control the flow of water should be partially closed to allow only a minimal amount of water so that the copper crucible doesn't melt while the sample was being arc melted. This however is not enough to allow the sample to slowly cool preventing the irreversible phase transformation discussed by Mozharivskyi et al. [38]

Once these changes were made, samples were able to produce consistently enough that they could be used in the manufacturing of GSG/PVDF devices that will be discussed in more detail later in this chapter. The samples that cracked and still retained crystalline structure were used in PVDF composites to be discussed later. These cracked pieces were further refined by crushing them between two aluminum plates in a rolling mill to make fine grains.

3.1.1.3. Melt Cycle Effects on Preparation

For the specific study of the effect of melting times on the microstructure of this material, three 1g samples were prepared in the same method. The only difference being the number of the sample is removed and melted. One sample was melted only 2 times, one was melted 4 times and one was melted 6 times. The samples were then mounted in Bakelite and polished using the standard metallographic polishing process that is described later in this thesis.

3.1.2. Polishing Process

All samples that were to be used for microstructure characterization were polished using the same process that is described here. The process is very simple and is a modification of the standard surface machining process. In essence the sample was ground until it has a flat and smooth surface.

The first step of the process was actually the last step of the arc melting process. The sample was cast during its last melt cycle in the arc-melting furnace in a flat bottom crucible. This flat surface was used for the polished one. The sample was polished using gradually increasing grit silicon carbide polishing pads, similar to standard waterproof sandpaper. The grit of these sand papers was 350, 400, 600, 800, 1000 and 1400. The pads were mounted on a Buehler Eco Met 2 series polishing wheel. The samples were moved in a circular pattern counter to the motion of the wheel by hand. This was done to minimize the amount of scratches that are present on the polished surface. Each step the surface was polished for approximately fifteen minutes before moving on to the next pad. The final pad used has 1400 grit and at this point the sample surface was near mirror like in appearance.

3.2. PVDF Composite Fabrication

In order to test the abilities of GSG to serve as a self contained thermal switch or monitoring system, a composte of PVDF and GSG was made. In leiu of more complicated film casting methods that produce a larger amount of material that would be more difficult to pole and test a simple spin coating process was chosen. This process was described by reference [70] in detail.

3.2.1. Solution Preparation

Solutions of PVDF were firstly prepared by dissolving bulk PVDF pellets purchased from Sigma Aldrich into a mixture of 20% DMSO and 80% acetone. The solutions contained 5 g of PVDF. The solution was heated on a hot plate to 50 degrees Celcius and aggitated by hand to allow the PVDF to fully dissolve in the solution. This heating however caused the solution of DMSO and acetone to evaporate which caused various viscocity solutions depending on the amount of time it was heated. Depending on the desired thickness, different dissovling times were used. A typical solution took 60 minutes to completely dissolve.

After the solutions were completely dissolved, measured samples of crushed $Gd_5Si_2Ge_2$ were added to the solution to create 1, 4 and 10 wt.% composites to test the activation of the $Gd_5Si_2Ge_2$. The ZnO powder was used to serve as a control. This powder was purchased from Sigma Aldrich and was measured to form the same concentration PVDF solutions as the GSG. The ZnO was a known piezolectic material.

3.2.2. Spin Coating

Solutions B1 through 7 were used for the fabrication of the spincast samples. The naming and conditions of samples are described later in this chapter. The spin coater used was Laurell WS-400B-6NPP, which is capable of achieving speeds of up to 5,000 RPM, while still allowing a varity of substrates to be used. The setup is shown in Figure 6.

Figure 6 Image of the spin coating system.

A drop, approximately 10 milimeters in diameter, of PVDF/GSG composite
solution was placed on a 1" (25.4 mm) diameter glass cover slide and ran the spin coater
at 1,000 RPM for 15 s. The samples on the glass slides varied in shape but typically
covered the glass slide. Figure 7 below shows the PVDF samples during different stages
in the production process.

Figure 7 Images showing PVDF in the different stages of production. Top left shows PVDF and GSG in the acetone/DMSO solution. Top right shows the product after spin coating and drying. Bottom shows the final product after poling, metal coating and protection in adhesive tape with leads attached.

At this point the PVDF samples are still saturated with the DMSO and acetone solution that must be removed. Several different combinations were tried in order to remove the excess solution. It was found that the best method of drying the samples is to rinse the samples briefly in acetone in order to remove the DMSO and acetone. Then very quickly rinse them in de-ionized water. The de-ionized water causes the organic solvents to be completely removed very quickly but the sample can also buckle quickly. Care must be taken to ensure that water is only applied for a brief period of time to not allow the sample to buckle.

3.2.3. Corona Poling

For PVDF to be an active piezoelectric material, it must be poled using a high electric field. In corona poling a high voltage is applied to a wire suspended over a grounded plate. This high electric field orients the polymer chains in their crystals so that when strained they will produce their own electric field.

3.2.3.1. Corona Poling Process

The samples were poled using a custom-built corona poling machine. The machine was made of 6061-aluminum so that there is a bar that holds the poling wire in a variable height above the sample, typically 3-5 mm. The whole system was designed so that in the event of a problem the high voltage poling wire would touch some part of the aluminum framework or casing that is grounded to serve as protection against electric shock. The sample is heated using a 6" by 6" (152.4 mm by 152.4 mm) 3M Kapcon heating pad that is affixed directly to the base plate of the poling apparatus. Shown below are images of the setup.

Figure 8 Images showing the poling set up and sample placement. The left image shows the entire setup. Right image shows the red poling wire above the sample with the thermocouple behind it. The sample is placed directly on the kapcon-heating pad.

The corona poling system uses a Buchler high voltage power supply attached to a 32-gauge wire. The base plate is grounded and the heating pad is powered with a variable transformer so that a sample can be placed directly under the poling wire with a gap of 3-5 mm for normal operation but as far as 1 cm for larger sample poling. A K-type thermocouple attached to a VMR thermocouple reader is placed in contact with the heating pad to monitor the temperature of the sample. The variable transformer applies power to the heating pad to about 70 % of the power of a standard electrical outlet (120V 60Hz), which typically heats the sample and heating pad to 150 degrees Celsius in a few minutes. Once the temperature has been stabilized at 150 degrees, the high voltage power supply is then turned on to 1000 volts DC and the sample is poled for 60 seconds. The power to the heating pad is then lowered so that the temperature of the sample and system falls to room temperature in 30 to 45 minutes. Shown in Figure 9 is a diagram of this type of system. On the right is the power supply and the wire is positioned above the sample on the left. The bottom plate of the capacitor is shown in the Figure but in reality it is the entire base.
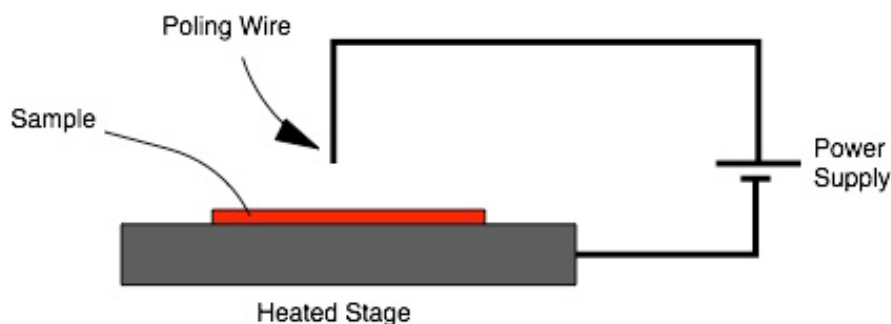
Figure 9 Diagram of poling setup. High voltage power supply is shown
on the right and is connected to the heated stage and poling wire. The
sample being prepared serves as the dielectric in the capacitor that is
being charged here. No resistor is needed as in traditional RC charging
circuits because of high resistance of the capacitor itself.

3.2.4. Metallization

To detect the electric field produced by the PVDF a metallic coating must be

applied to both sides of the polymer films without a short circuit. It can function as a

capacitor with the PVDF in the middle as a dielectric. A sufficiently thick and robust

layer is required. Thermal evaporation, sputter coating and metallic inks have all been

used with great success. For this study, thermal evaporation was used because these

facilities were readily available.

The samples were coated using a BOC Edwards Auto 306 Metal Evaporation

Chamber. A thin layer, approximately 100 nm thick, of chromium was applied to the

sample since the heat required to deposit a layer of chromium is about 50 degrees

Celsius which is well below the temperature at which the sample could loose its pole.

Other metals require a temperature that could be damaging to the material.

At this point the sample edges were trimmed to ensure that the two metal films did not short circuit the system. Electrodes were attached and the samples were wrapped in a protective polyethylene adhesive tape. This tape was simply folded on itself such that the sample and electrodes were in between. This tape serves to keep the system together as well as protect the fragile PVDF film.

3.3. GSG/PVDF Sensing Element

To effectively monitor the behavior of GSG for use as either a refrigerant or a thermal switch there must be a way to attach a monitoring system to it. This involves attaching a solid piece of GSG to a film of PVDF to serve as the sensing device. A variety of methods were attempted resulting in a final working device, which was tested and will be reported later.

3.3.1. Constructing Sensing Device

For the purposes of this study, pre-manufactured PVDF sheets provided by Measurement Specialties were chosen. Three 8 ½" by 11" sheets were purchased in different thicknesses, 28, 52, and 108 microns. Each sheet was electro-statically poled, stretched and coated with silver on both sides by the manufacturer. While all the sheets exhibit a strong piezoelectric response, each thickness has a specific application. The thicker 108-micron film is best for situations where physical robustness of the same film is required. This is especially useful in applications where the PVDF film will experience strong mechanical strain and repeated deformation. The thinner 28-micron film is best in situations where sensitivity or geometric limitations are key. The 52-micron film is a good middle ground between these two extremes and is most applicable

to most uses. All three of these films were tried in all of the different versions that will
be discussed next. It was found that the sensitivity of the 52-micron film was most
advantageous for this application.

3.3.1.1. GSG/PVDF Sample Preparation

First a sample of GSG was arc melted using the method described above and on
the last melt a flat bottom crucible was used to facilitate the easier polishing of the
sample. The sample was then polished with 320-grit silicon carbide sandpaper until the
surface was uniform in height and no pits remained on the surface. Then the sample was
polished with increasingly finer polishing pads until the surface was shiny but still
contained significant scratches visible to the naked eye. The high surface roughness of
the sample provides a means of transferring the strain caused by the phase
transformation to the PVDF.

3.3.2. Progression of Versions of PVDF/ GSG Systems

For each version of the system at least three different types were made. One with
a 1 gram GSG sample, one with a 2.5 gram GSG sample, and one with a approximately
3 gram sample of steel. The steel sample serves as the control and shows the interactions
between an inactive material and the PVDF.

3.3.2.1. Version One

The first version of the PVDF/ GSG system involved a very simple setup. Once
the GSG sample was prepared and polished properly the sample was attached with
cyanoacrylate on top of a piece of PVDF that had leads attached to it. This produced a
system where the GSG sample was asymmetrically attached to the PVDF, which did not

allow good adhesion between the two materials. A diagram of this set up is shown in

Figure 10. Further problems with this set up will be discussed later.
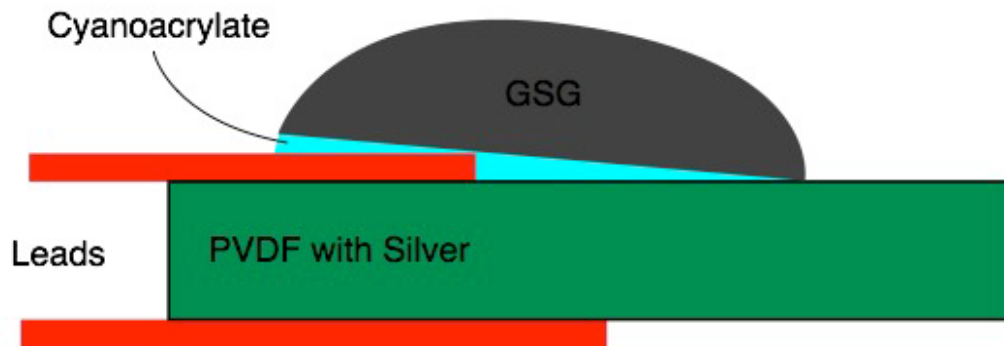
Figure 10 First version of PVDF/GSG system.

3.3.2.2. Version Two

Then next progression of this set up involved moving the leads on the PVDF out

from underneath the GSG sample, this set up produces greater bonding between the

sample and the GSG and will serve as the basic format for the rest of the following

designs until complete integration of the materials is achievable. Below is a diagram of

this system.
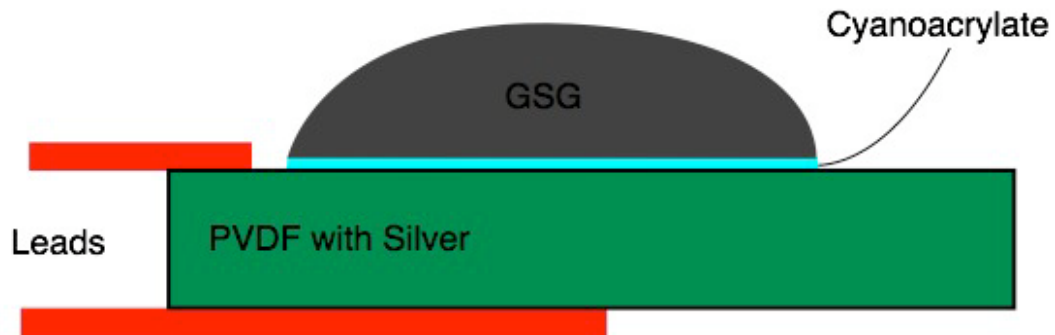
Figure 11 Second version of PVDF/GSG system.

3.3.2.3. Version Three

Problems with the adhesive led us to replacing the cyanoacrylate with M-Bond adhesive. M-Bond is a two part solvent thinned epoxy with a large useable temperature range from about -250 to 350 degrees Celsius. This wide temperature range allows us to cool the system with a variety of coolants ranging from liquid nitrogen to cold plates. The next version of the system involved simply replacing the cyanoacrylate with M-Bond. A diagram of this is shown below.
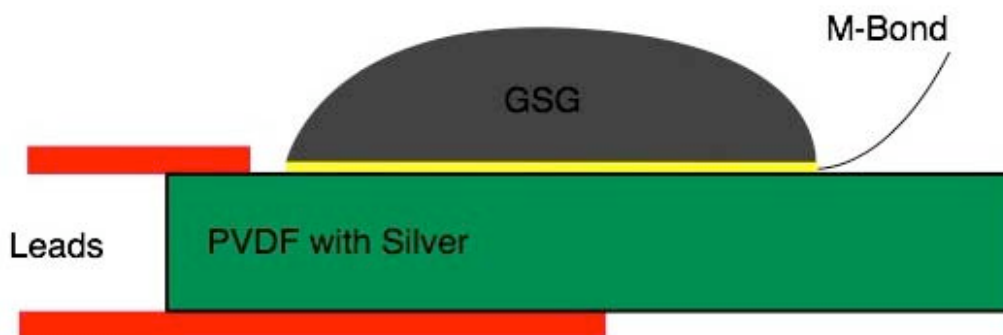
Figure 12 Third version of PVDF/GSG system.

3.3.2.4. Version Four

To simplify the system further, the printed silver was removed from the PVDF. The new design now called for the removal of the silver by gluing the sample to the PVDF with the silver printed on with cyanoacrylate. Then the sample and the attached silver were peeled off. The sample was then cleaned with acetone to remove the cyanoacrylate and then reattached with M-Bond. A diagram of this set up is shown below.
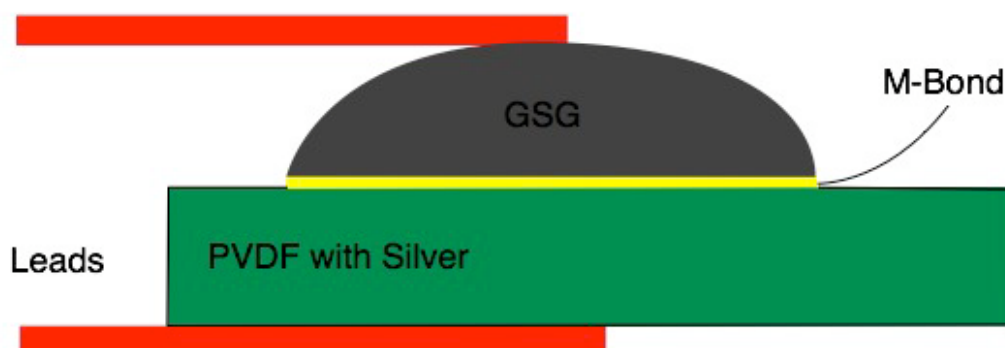
Figure 13 Fourth version of PVDF/GSG system. Note the removal of
the silver coating (black line) from the area under the GSG.

3.4.   Electrical Testing Method for PVDF/GSG and Composites

The electrical testing methods for these systems have undergone significant

improvement since the first versions of the system. The first versions of the GSG/PVDF

samples were cooled by immersing them in liquid nitrogen, while their temperature was

monitored by a thermocouple. This caused a large pyroelectric effect that, in many cases,

masked the interaction of the GSG with the PVDF. Differences in cooling rates in this

system also produced a great deal of problems when trying to monitor the temperature

because the thermocouple would often read much lower than the actual sample

temperature. To remedy these problems, it was decided to cool the samples on a bed of

dry ice. The high temperature of dry ice reduces the thermal shock, which leads to the

pyroelectric effect in PVDF and also allowed the thermocouple and sample to cool at a

similar rate.

For these studies the sample is connected to a National Instruments USB-6229

DAQ board along with the thermocouple. The thermocouple is attached to the sample

using adhesive tape on the PVDF side of the system. The sample is cooled by placing the GSG side of the system in contact with the bed of dry ice and then securing it with a weight attached to a foam block. This foam block allows the system to be secured in any position without disturbing the PVDF during testing. A Labview 8.6 program built then records the voltage produced by the PVDF and the temperature of the thermocouple and records it in a text file.

3.5.   Sample Labeling

All samples, composite, and GSG, used the same standard form for labeling. The name consists of two parts a batch number and a sample number. A letter indicates the batch number and a number indicates the sample number. So a sample has the label "B2". This means that the sample was from the second batch (B) the second sample of that batch (2). The first samples made have a lower batch number than the later ones.

GSG samples started the batch numbers with "A" and continued to batch "I". The different batches contained samples of different sizes and for specific tests. The size of the sample will be noted when describing the sample

The composite sample batches were labeled from S to Z and then AA in the same system as the GSG samples. The samples themselves were numbered by the order of manufacture. Each batch had a different concentration of filler material. Again the batches that were made were on an as needed basis and the names are not linked to the concentration of filler material. Table 5 below shows a list of the different samples made and the properties of each batch.

Table 5 Table showing the different sample batches and their properties.

Batch	Sample Type	Size or Filler %	Other Comments
A	GSG	10g	
B	GSG	5g	
C	GSG	5g	
D	GSG	1g	
E	GSG	2.5	
F	GSG	5g	
G	GSG	3g	
H	GSG	3g	
I	GSG	1g	Different Melt Times
S	GSG Composite	4%	
T	Pure PVDF	0%	
U	Pure PVDF	0%	
V	GSG Composite	1%	
W	ZnO Composite	4%	
X	ZnO Composite	10%	
Y	GSG Composite	4%	
Z	GSG Composite	10%	
AA	ZnO Composite	1%	

3.6.   **Materials Characterization**

This section describes the various experimental techniques and procedures used to characterize the materials produced above. As mentioned before these techniques will be descried in theory then in practice. X-Ray diffraction was used for the simple crystallographic study of all samples while the other techniques were used to study the microstructure of these materials. It should be considered that the X-ray diffraction studies confirm the composition of these materials while the others focus on their physical properties.

3.6.1. X-Ray Diffraction

3.6.1.1.   Background

X-Ray Diffraction, XRD, is a powerful nondestructive technique that allows the accurate determination of the crystal structures of a material. Analysis of XRD data can be complicated especially on materials that have complicated multiphase structures like $Gd_5Si_2Ge_2$. This research will be limited to simple comparisons and simple calculations of the crystal planes.

XRD works by monitoring the scattered x-rays from an incident x-ray beam on the surface of a sample. The X-ray beam is typically monochromatic to limit the errors produced by multiple X-ray energies interacting with the sample. As the beam interacts with the crystal structures in the sample they are scattered off by the different planes present in the crystal. The scattered beam is monitored by a moving detector on a goniometer that measures the intensity of the x-rays at different angles denoted in terms of two-theta. The Figure 14 is a diagram of the XRD technique.
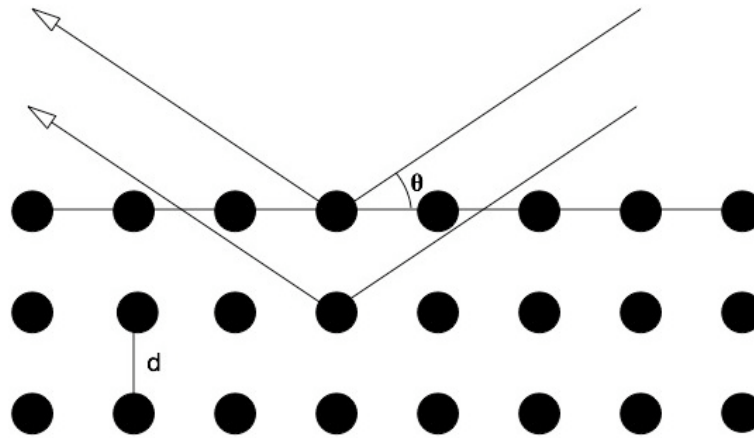
Figure 14 Diagram showing the behavior of the reflected x-rays from the sample surface.

Each crystal plane interacts differently with the x-ray beam and scatters the X-rays at its own specific angle. From this angle we can determine what plane of the crystal it corresponds to and by looking at the sum of these planes it is possible to tell what kind of crystal structure is present in the sample. Since this is not a surface sensitive technique it can be used on all samples, polished or unpolished. The detector only monitors the angle and the intensity the data output from the XRD system. Data are typically plotted as a graph of the angles in a specific range and their corresponding intensities, similar to the one for copper in Figure 15. By looking at the relative intensities of the peaks in different phases in the material it is possible to get a rough estimate of the amount of each phase in the material.

*Copper-Cu-[FM3-M]Swanson, H.E.;Tatge, E.[1953]
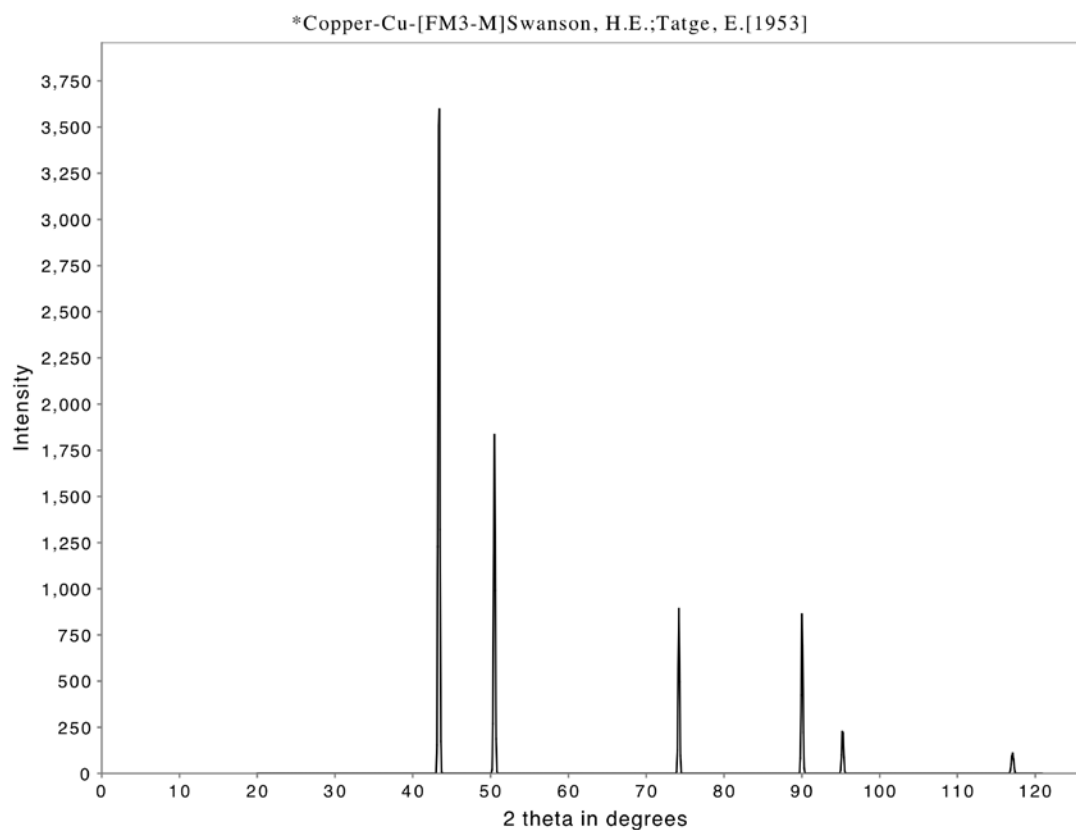
Figure 15 Two theta plot of FCC Copper.[71]

3.6.1.2. X-Ray Diffraction Procedure

For this study the Bruker-AXS D8 Advanced Bragg-Brentano X-ray Powder Diffractometer maintained by the user facility in the Texas A&M University Chemistry Department was used to study the crystal structure of GSG. This particular machine uses a standard 250 mm two-circle goniometer in order to vary the angle of the x-ray beam. The x-ray source is a standard copper emitter. This machine is computer controlled and

collects the data automatically in a file that can be read by Microsoft Excel.

For the purposes of our experiments the step size was set at approximately 0.15 degrees and the tests were run on a typical range from 5 to 70 degrees and the time was set so that the run could be completed in approximately eight minutes. These parameters provide good resolution and a range that allows comparison of these samples to the vast majority of published data.

The data were then processed using the X-ray diffraction program EVA, produced by the Bruker Corporation. Using this program the peaks were located and marked using Bragg's law. The XRD pattern was then smoothed using an automated Fourier transform process. Then the background contribution was removed from the pattern using the background analysis tool. Then the data is ready for presentation or further analysis using the expected plane spacing.

To identify which peak corresponds to which crystal plane, the formula for the expected crystal plane spacing is used. This formula is filled in with the published information of the crystal lattice parameters published by Pecharsky et al. [21] The crystal planes are then guessed and checked against the existing peaks in the XRD pattern collected. Once a suitable match is found, that peak is labeled as that crystal plane and the process continues until all the peaks detected by the software have been labeled.

All of the samples that were arc melted were run under these conditions to ensure that they were the proper crystal structure and had similar phases to that of the published data.

3.6.1.3. Long Term Crack Investigation

To determine what crystal structure changes caused the long term cracking, twelve

samples were arc melted, four 1 g, four 2.5 g and four 5 g, and immediately analyzed

with XRD to see their crystal structure right after arc melting and then wait several

weeks to see if any of the samples cracked and decomposed into a powder and then

perform XRD analysis on them again to measure the change. After four weeks only one

1 g, one 2.5 g, and three 5 g samples had cracked and decomposed to the point at which

it could be reasonably assumed that they had changed crystal structures. These five

samples had XRD analysis conducted on them and that was then compared to the

original XRD results.

3.6.2. Atomic Force Microscopy

3.6.2.1. Background

Atomic force microscopy is an extremely powerful technique for studying the

surface structure and morphology. It allows a great deal of information to be obtained

about the surface features and relative mechanical properties.

AFM works by moving a small cantilever with a needle like tip in a regular

pattern across the surface of the sample. The tip typically is pyramidal or conical in

shape and has an end diameter of approximately 10 to 50 nanometers depending on the

quality, age, usage, and purpose of the tip. The position of the tip is monitored by the

interference patterns produced by a focused diode laser that is positioned on the end of

the cantilever. As the cantilever moves up and down the laser light produces interference

patterns that a photo-detector detects and then relates back to the height of the tip. A

diagram of this set up is shown in Figure 16.
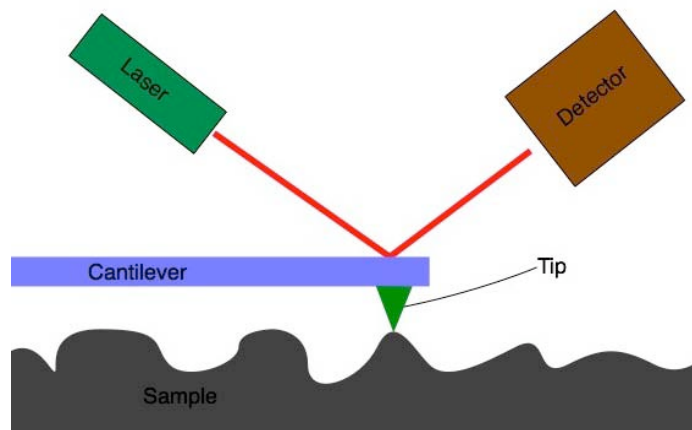
Figure 16 Diagram showing the mechanism of AFM.

There are two typical modes of operation for AFM scans. The first, and the most simple, is the contact mode. The tip is in direct contact with the surface of the sample and drags along the surface like a needle on a phonograph. While this mode of operation provides a clear picture of the surface it tells little about the material differences and greatly reduces the lifetime of the tip. The second, and the most common mode of operation is tapping or intermittent contact mode. In this mode the tip is driven to oscillate at its natural mode of oscillation and is brought close enough to the sample that it strikes the sample at the bottom of each oscillation. The sample is then moved in a raster pattern to map the surface as the tip encounters differences in height it changes its oscillation, which is monitored by the system. The size of this pattern is typically on the order of a few microns but can be as large as 70 microns depending on the abilities of the instrument. Typically large scans show more features but have less resolution, while

small scans have higher resolution with less features. This phenomenon is due to the

nature of digital systems and the tapping mode of the tip.

Any interaction with the sample surface will exchange energy with the tip and

cause a change in the phase of the oscillation. If the sample is hard, the sample will

exchange less energy with the tip as it strikes the sample than if it were a softer material.

Since differences in material can change the amount of energy and therefore the phase of

the oscillation of the tip, it is possible to use this fact to get a relative difference in the

materials. A diagram showing the changes in oscillation is shown in Figure 17.
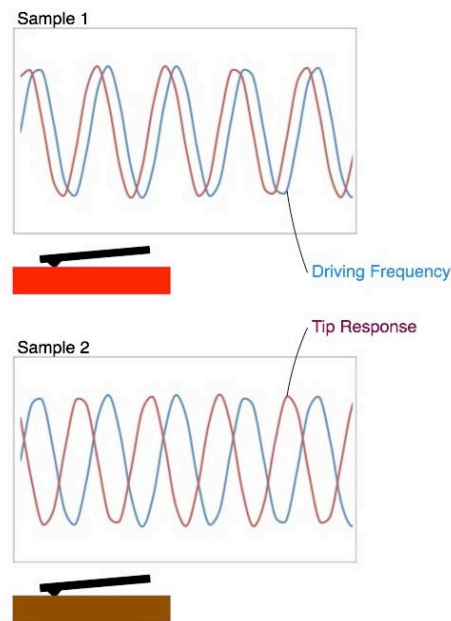
Figure 17 Diagram showing the phase offset of different materials in
the AFM. The tip is driven by a signal represented by the blue line but
the red line gives the actual tip response. The difference is caused by
exchange of energy with the sample.

It should be noted however, that there are limitations to this effect. First and foremost since each tip will have its own natural frequency of oscillation and will be affected differently by changes in material, it is neither useful nor representative to compare the values in a phase image to those in another image. The results cannot be compared to one another; it is not useful to use these results as anything more than a rough comparison of differences in the material. Materials with similar properties appear the same in the phase image, whereas other techniques can show these differences.

3.6.2.2. Operating Procedure

For this particular study, a 1g $Gd_5Si_2Ge_2$ sample was chosen because it served as a good representation of the whole set of samples and did not exhibit any of the major cracking problems. This particular sample, D2, was arc melted four times with the last being in a flat-bottomed crucible. The surface of the sample was then ground flat to remove any major highs and lows off the surface. It was then ground on the other side to provide a flat surface to, care was taken to make these two sides parallel. The software can remove slight changes in slope without damaging or misrepresenting the data image. The sample was then prepared by the polishing process described below.

The sample was then tested with the AFM in all of the modes mentioned above in a variety of scan sizes. A Pacific Nanotechnology Inc. Nano-R AFM was used in the close contact mode for this study. The results of this study will be discussed later.

3.6.3. X-Ray Photoelectron Spectroscopy

3.6.3.1. Background

X-Ray photoelectron spectroscopy (XPS) is a surface chemical analysis

technique used to determine what kinds of elements are present in the surface of a

sample as well as the types of bonds that are causing interactions between the electrons

in the atoms. XPS works by bombarding the surface with high-energy X-ray photons.

When these photons strike the surface they excite the electrons in the atoms. These

electrons can become so excited that they are removed from the atom completely. The

number and energy of these electrons is detected by the system. The energy of these

electrons is the difference between the X-Ray photon and the binding energy of the

electron. The exact energy that is applied to the electron through the x-ray is known and

it's energy after it is removed from the atom it is possible to calculate its binding energy.

Since the binding energy can be theoretically calculated with great accuracy for each

electron in each element, precise determination of the constituent element is possible.

Additionally if there are any chemical bonds in the system those will pull on the

electrons differently and cause their binding energy to shift slightly. From this shift and

the presence of the other elements in the sample an accurate picture of the composition

of the surface is possible. While this technique does not provide the exact chemical

concentrations of complex compounds, it is useful for finding the chemical

concentrations of simple compounds. Combine this with the fact that it typically has a

penetration depth of only 1-10 nanometers; this technique is useful for studying the

oxide formation on the surface of a material. Data is typically presented in the form of a

spectrum of the electron energies and their respective intensities. Electronic bonding will lead to broadening of the peaks.

3.6.3.2. Operating Procedure

The particular instrument used for this study was a Kratos Axis Ultra Imaging X-ray photoelectron spectrometer. This instrument has two x-ray sources; a sodium source and a copper source since different materials respond differently to different energies of X-rays. The sodium source was almost exclusively for these tests. The hybrid lens mode was used in a single pass mode with pass energy of 80 eV. All other features of the system were set to automatic.

3.6.3.2.1.   Mapping Procedure

This instrument also has the ability to map the concentrations of different elements on the surface of the sample. This mode of operation is known as XPS mapping. It does this by conducting an XPS scan on a small region of the surface; typically an area equal to or slightly less than one micron, and then moving over one similar sized space and conducting a scan until the desired region is scanned. The software then identifies which elements are dominant in that region and it can generate a map of those elements.

In this study, sample D2 was reused and was only cleaned with acetone between tests. Several single-point studies of the surface were conducted and difference in the surface and the different features noticed with the AFM studies led to the use of the XPS mapping feature. It has been found that different changes in concentration can lead to changes in structure. Therefore XPS was used to see if there were large scale variations

Elemental maps of the surface were conducted by setting the system to select the desired element and setting the timer per point at 200 ms. All other settings were chosen to be the same as the single point study described earlier. Three different scans were conducted using selected Gd, Si or Ge for each run.

3.6.4.   Scanning Electron Microscopy

3.6.4.1. Background

Scanning electron microscopy (SEM) is one of the two main electron microscopic techniques commonly used in materials characterization. For this technique, electrons from a tungsten filament are excited and removed from the surface by heating with an electric current. Tungsten is commonly used because of its low cost, high melting point and low vapor pressure when compared to other metals. The excitation voltage applied to the filament determines the energy of the electrons. Once the electrons are excited off the tungsten filament they are focused using two focusing elements that focus the beam down to an area of ranging from one angstrom to 5 nanometers. The size of this area will determine the quality and resolution of the microscope. The beam is moved in a raster pattern by a pair of electromagnet coils that move the beam over by applying a magnetic field that induces a Lorentz force on the electrons and diverts their path. A diagram of this setup is shown in Figure 18.
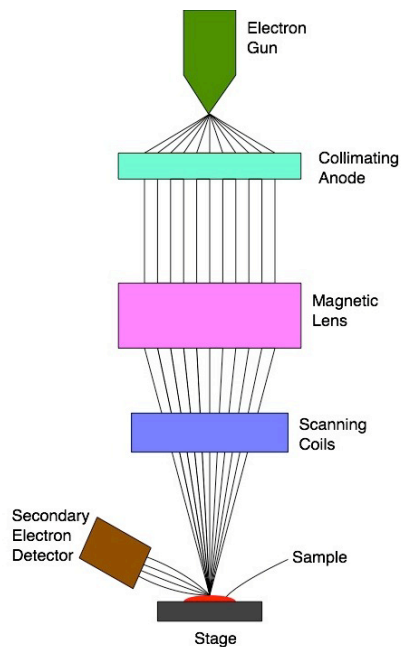
Figure 18 Diagram of the mechanism of SEM.

As shown above, the sample is placed at the end of the electron beam. As the

electrons interact with the surface of the sample they remove electrons from the outer

energy levels. An electron detector measures the intensity of the resulting beam and

plots this intensity in the image. This process, called secondary electron imaging,

provides the image that is typically seen on the SEM readout.

This technique, because of its dependence on the electronic properties, the small

beam size and depth of field, provides a great deal of information about the surface of

the sample. The SEM technique usually requires that the sample is conductive so that

there is not a charge build up on the surface. Charge build up causes the electrons to

immediately be repulsed by coulomb forces resulting in a poor image. Many samples

that could benefit from SEM are often not conductive so it is quite common to use a sputter coater or thermo-evaporator to coat the surface of the sample with a thin layer of metal.

3.6.4.2. Other Imaging Techniques

While the secondary electron imaging is the primary process for imaging with SEMs, the technique also provides a great platform for the application of other techniques. One of the more common techniques typically used is the detection of backscattered electrons. In this technique the electrons that undergo elastic collisions with the surface are detected and this intensity forms the image. Since elements with higher atomic numbers backscatter more electrons than lower ones, this technique is very sensitive to changes in composition. Other techniques like cathodoluminescence, electron current and x-ray microanalysis can be used if the test requires.

3.6.4.2.1.   Energy Dispersive X-ray Spectroscopy

Energy dispersive x-ray spectroscopy, EDS, was used to study the elemental composition. When the electron from the beam interacts with an atom it can eject an electron causing a higher energy electron to fill that energy level. In the transition the electron emits a characteristic x-ray photon that is detected by this technique. Each element has its own particular photon energy and is well known. Then the software can create a map of this information and give a detailed image of the surface chemical composition.

3.6.4.3. SEM Procedure

A field emission electron microscope was used to study the surface of the same sample that was used in the AFM studies. A field emission microscope simply uses a

different type of electron gun that produces a narrower beam that results in higher resolution and higher possible magnifications. For this study we used a JEOL JSM-7500F field emission SEM that was equipped with an Oxford EDS system for elemental mapping on the surface. This machine is automated requiring that the user only selects the electron beam energy and focus the machine. Sample D2 was used again for this study. The electron beam was excited using 20kV and adjusted so that the image produced was clear and in focus.

EDS on this system is also automated so that the user only has to select the EDS feature and let it collect until a sufficiently clear image is produced. Gd, Si, Ge, O and Cu were selected for the elemental mapping because these elements were expected to be prevalent in the material from the processing conditions. EDS studies were done on the same areas that were tested using the secondary electron images. The scans were allowed to run until the image clearly showed the major features noticed with the secondary electron image.

3.6.5. Optical Microscopy

After the AFM, XPS and SEM studies of the surface of GSG low cost ways of studying the surface of the material and determining the different phases quickly without costy sample preparation and equipment were considered. High powered optical miroscopy was the obvious choice for this role. A Keyence VHX-600 digital optical microscpe and a high power lense that is capable of up to 5000 times maganification without any digital enhancement was used to study the features of the materials. The sample D2 was again used for this study. First, as mentioned above, the surface of the

GSG was observed to see if any of the effects that were noticed in the AFM and SEM pictures could be noticed using a lower cost and less intensive microscopy technique. It was also used to study the effects of melt times on the microstructual properties of the GSG using the samples that were arc melted two, four and six times as described above.

3.6.5.1. Image Analysis

Image analysis software,ImageJ [72], was used to calcualte the average partical size and the interpartical distance that was then used to find out the dispersion of the partices and their relations to the matrix material. This process is done by converting the image to a binary image using the built in features. Then an image processing algorithim to select regions that of spots versus the empty regions is used. The scale bar of the image is then used to create a reference of how large a single pixel is. Then an image report is generated by the program that compares the areas, average sizes and number of features versus blank area. This data is presented in a table for the user.

CHAPTER IV

RESULTS

This chapter presents the results from the synthesis of the GSG-PVDF composite materials and devices and the analysis of various properties of the same. It starts with the materials, and then devices made, and their performance. Followed by the investigation in to the microstructure of as-cast GSG and effects of processing conditions on the microstructure of these materials.

This section confirms the piezoelectricity of the spin cast PVDF film and characterize the power produced by these films when they respond to the phase transformation of GSG. Both the power produced by the GSG and the ZnO control are presented. Additionally, the power produced by the PVDF/GSG devices is presented as well as a discussion of each version of the system's performance.

4.1. GSG/PVDF Piezoelectricity

Solutions of PVDF were made and mixed with 1, 4, and 10 % by weight of crushed GSG or ZnO powders. These powders were crushed to an approximate particle size of 1 to 5 microns. Firstly the samples were tested to ensure that they produced a noticeable voltage due to the piezoelectric effect. This was done by attaching the sample to a voltage monitoring system and applying pressure to the PVDF by squeezing it between the forefinger and thumb. This setup is described in Chapter 3 section 1.5.3. The results of this confirm that the poling process was successful. Shown in Figure 19 is a graph of the voltage produced as it was compressed. The X-axis is the time in seconds of a particular testing section and Y-axis is the voltage produced by the PVDF film as it

is compressed. It shows that the material produces a changing voltage depending on the

actuation pattern. Since this situation was loaded by hand, it is extremely hard to give an

exact loading scenario. Roughly, the sample was compressed in a sinusoidal pattern.
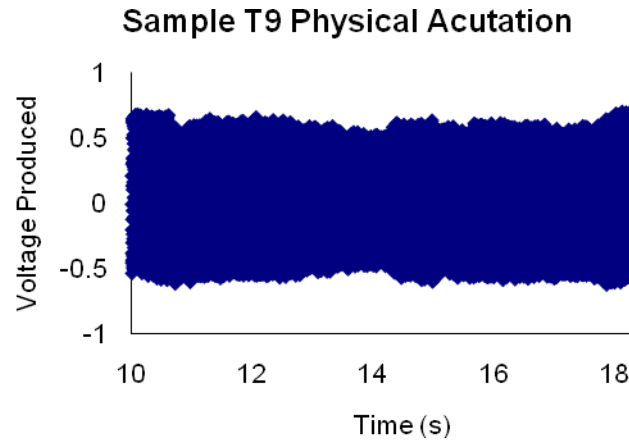
Figure 19 Excerpt from test of the piezoelectricity of a pure PVDF
sample, this particular section shows a time span where the sample was
compressed between the forefinger and thumb in an attempted
sinusoidal loading pattern.

4.2. Power Calculation

To calculate the power produced several assumptions had to be made. Firstly the

power was calculated using its definition. With the current replaced with Ohm's law.

This process is a well-accepted means of calculating electrical power passing through a

resistor:

$$P = VI = V\left(\frac{V}{R}\right) = \frac{V^2}{R}$$

P is the power produced by the PVDF. V is the voltage produced, I is the current produced and R is the resistance of the sample. The first two expressions are the definition of electrical power. The third expression is the substitution of Ohm's law for the current that results in the final expression of power as a function of the square of the voltage divided by the resistance.

The voltage is measured but the resistance of the films must be calculated from the bulk resistance of PVDF. For this term, the volume resistance of PVDF was used. Volume resistance is a material property that gives the resistance to current flow of a 1 cm block of the material; it typically has units of ohms/meter^3. For PVDF the volume resistance is 1.5×10^{14} ohms/m^3.[18] To calculate the resistance of these particular films the volume resistance was multiplied by the volume of the film. This is the value that was used in the calculation of the power produced in the by the system. To find the volume of the films the height was measured using a contact profilometer and the area was measured using a flat bed document scanner. This process will be described in the next sub-section.

For the power calculation of GSG composites and devices the power was summed over the region in which the PVDF was responding to the phase transformation of the GSG. This area was selected by hand but is an extremely clear area and is not significant source of error. For the control composites and devices, ZnO and steel based systems; the average power was used since there was no response that could have been summed.

4.2.1. Sample Thickness Considerations

The thickness of the sample was measured by using a Qualitest stylus profilometer by measuring the height of the sample relative to the glass slide that the sample was spin coated on to. The result of this process is similar to the curve in Figure 20.
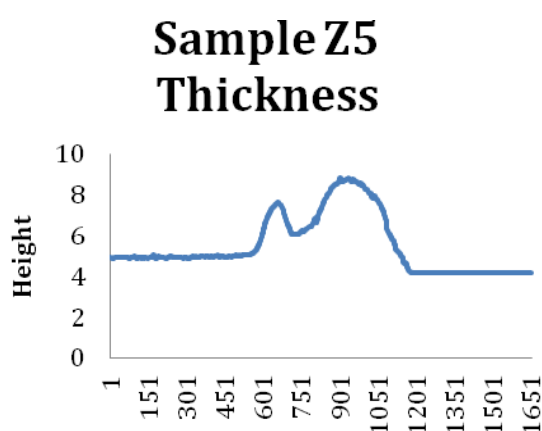
Figure 20 Height scan of a 10% GSG composite film. The nearly flat and smooth region from 1 to around 554 is characteristic of the center of the sample, while the region from 1186 to 1581 is the glass substrate slide. The two higher regions are from where the material built up on the extreme edge of the sample during spin coating. Height is determined by subtracting the center region from the height of the glass substrate.

The average height of the region on the sample was then subtracted from the average height of the glass slide and the difference is the thickness of the sample. A table of average thicknesses of the different samples for both GSG and ZnO is shown in table 6. This table shows the average thickness of different samples depending on the type and concentration of filler each average is of three different samples. Note that due to the

destructive nature of the test, these are samples from the same batch as the samples used

for power testing but not the same samples. They are very similar in dimensions as the

other samples

Table 6 List of thickness of samples measured.

Average Thickness (in um)						
Pure PVDF (Series U)	1% GSG (Series V)	4% GSG (Series Y)	10% GSG (Series Z)	1 % ZnO (Series A)	4% ZnO (Series W)	10% ZnO (Series X)
2.677±0.893	5.77±3.800	5.338±2.339	9.78±1.667	8.594±0.245	2.099±0.994	11.104±4.762

Using the image analysis program ImageJ and a flatbed document scanner the

areas were calculated. The composite was scanned into an image and the size of the

devices were calculated in pixels, which was then converted into a real area. Table 7

shows the areas that were found for all of the samples used. These values along with the

thicknesses were used to calculate the power produced by each sample.

Table 7 Area of the composite films in cm^2.

ZNO 10%			ZNO 4%		
X2	X1	X3	W3	W1	W2
0.906	1.0	0.716	1.278	1.32	1.101
ZNO 1%			GSG 10%		
A3	A2	A1	Z3	Z2	Z1
1.774	1.806	2.611	1.242	1.89	1.737
GSG 4%			GSG 1%		
Y1	Y3	Y4	V3	V2	V1
1.418	1.355	1.459	1.554	1.146	0.981

4.3. Electrical Power

These experiments were conducted on both the composite and PVDF/GSG
device systems using the standard dry ice method described in the experimental section.
Each system was tested at least three times and three samples were used for each test.

4.3.1. Composites

Samples were prepared with 1, 4, and 10 percent by weight GSG. While each one
showed different amounts of this effect it was clearly noticeable and first tested on the
4% GSG sample. The samples were measured in the same manner as the last
PVDF/GSG system. Figure 21 shows an image of a finished film before testing.

Figure 21 Image of the final PVDF/GSG Composites.

Figure 22 is a graph of the 4% GSG sample while being cooled on dry ice. In this

Figure the X-axis is the temperature of the thermocouple and the Y-axis is the voltage

produced by the PVDF film as it is cooled with the dry ice.
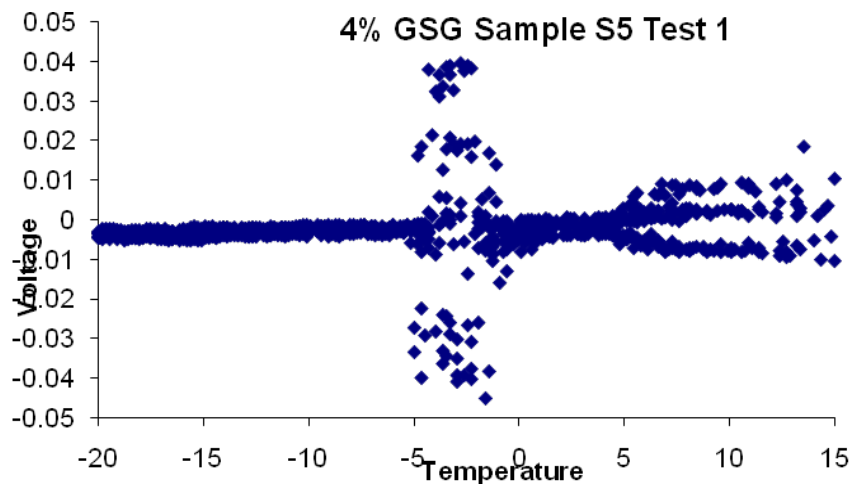
Figure 22 Voltage vs. temperature for sample S5 which contains 4 wt%
GSG. Increased voltage signal is residual pyroelectric effect from the
cooling of the PVDF but has no significance on the power produced by
the system.

The graph shows a clearly noticeable peak around -4 degrees Celsius. This is the region that GSG typically undergoes its phase transformation without an applied magnetic field. In the absence of any other applied forces there should be no other reason for this voltage to be produced other than the phase transformation resulting large thermal expansion of the GSG.

To confirm this effect, a comparative study was conducted. ZnO was mixed into the PVDF solution in the same concentrations as the GSG. These samples were then tested under the same conditions as the GSG samples and produced no noticeable voltage in the same region as the GSG composite. Figure 23 is a graph of the voltage produced by a 4% ZnO sample as it was cooled with dry ice.
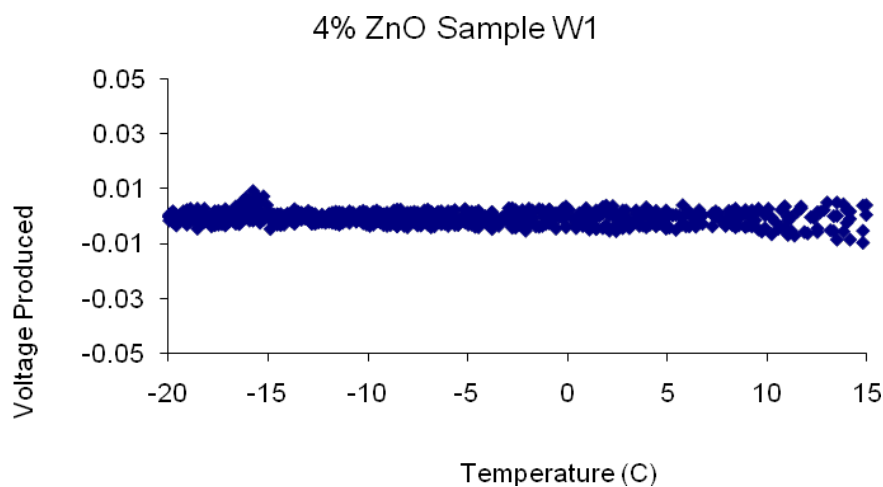
Figure 23 Voltage vs. temperature graph showing the lack of contribution of ZnO. This particular graph shows the response of sample W1 which contains 4 wt% ZnO.

While these charts show that this method of detection of the phase change of GSG, they do not show the effect of concentration on the voltage produced. In order to test this effect the concentration was varied and tested under the same conditions for all samples. Shown in Figures 24 through 26 are voltage graphs produced by each concentration of sample, 1, 4 and 10% GSG.
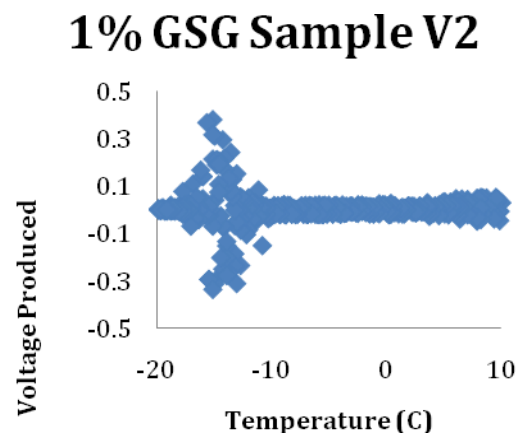
Figure 24 Voltage versus temperature graph for a 1% GSG composite film. Temperature shift from -4 C to ~-15 C is caused by a lack of good thermal transfer between the sample and thermocouple.

4% GSG Sample Y3
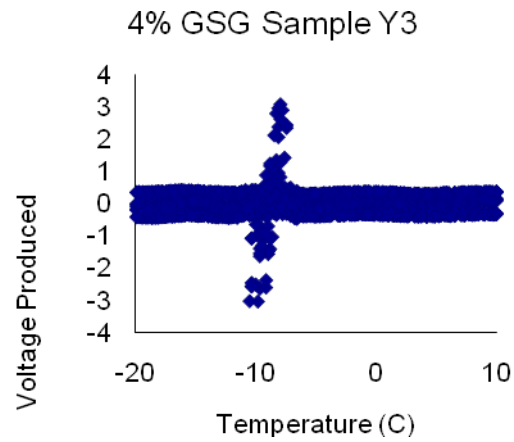
Figure 25 Voltage versus temperature graph for a 4% GSG composite film.

10% GSG Sample Z1
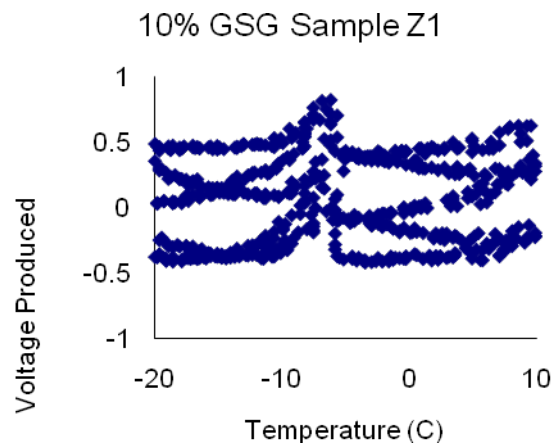
Figure 26 Voltage versus temperature graph for a 1% GSG composite film. The large error in this test is caused by the pyroelectric effect and instrumentation problems but is resolved in the final power considerations when the sum and averages are considered.

4.3.2. PVDF/GSG Device

This section describes both the reasons for the development of the different versions of the PVDF/GSG systems, as well as the electrical testing of these systems. Electrical testing is presented in two different subsections; initial results that show the possibility of this kind of system as well as a section that describes the power produced by the final system. It should be noted that the initial results were produced by version two of this system and were the encouragement for the exploration of the other.

4.3.2.1. Device Versions

In the experimental chapter, several different versions of PVDF/GSG monitoring systems were described. Each version has its own focus in design consideration. This section discusses the unique features of each system and attributes of each version of the system.

The first version of the system was simply a piece of GSG attached to a small piece of PVDF with cyanoacrylate with the leads attached in a sandwich type arrangement, as shown in Figure 10 in chapter 4. This setup was initially chosen because it ensured good electrical contact between the PVDF and the voltmeter and was fairly robust at room temperatures due to its integration with the cyanoacrylate. Initial tests with this system involved cooling the setup by immersing it in liquid nitrogen. When placed in the liquid nitrogen the thermal shock combined with the thermal contraction of the GSG caused the cyanoacrylate to become brittle and the sample to fall off.

The next version involved moving the leads out from underneath the sample and to the side of the PVDF, as shown in Figure 11 in chapter 4. This change doesn't cause a difference in the electrical connection since the silver printed on the PVDF is thick

enough that it is robust enough to withstand having a sample attached to it. This system was effective or the PVDF to give a response under a single test. This system proved that this device is feasible for multiple tests but it points out the need for good adhesives.

Since bonding is one of the major challenges in device development. The version shown in Figure 12 in chapter 4 focused on adhesion. It involved replacing the cyanoacrylate with M-Bond adhesive. This change greatly improved the thermal resistance and the lifespan. The systems typically lasted for about 10 cooling cycles. These systems also removed the silver from the PVDF film.

The next and ultimately final version of the system involved removing the silver from the PVDF and using the sample itself as the conductive surface for the PVDF. A diagram of this system is shown in Figure 14 in chapter 4. This system works very effectively for creating a reliable, consistent and reusable system to act as a thermal cycle monitoring system. The next sub-sections detail the results of the final system. At this point in the testing liquid nitrogen was no longer used to cool the samples but was replaced with dry ice. Dry ice has a lower temperature and doesn't induce as high a thermal shock in the sample and is easier to work with than liquid nitrogen. The final version of the device functions both with dry ice and liquid nitrogen but testing is more reliable with dry ice.

4.3.2.2. Power Production

Once the final system design was chosen power testing on the final systems was conducted. Firstly, three different versions of the device were manufactured; a 1g GSG, 2.5g GSG and steel system. The 1g and 2.5g samples both use samples of GSG but the sample size was changed to test for contact area effects. The steel sample was made as a

comparative sample. The testing was conducted in the same dry ice method used on all

other samples, which is described in chapter 4 section 1.5.3. A graph of the voltage

results for a 2.5g device is shown in Figure 27 below. As in the composite results, the X-

axis shows the temperature of the thermocouple as the sample is cooled on dry ice, while

the Y-axis shows the voltage produced by the PVDF.
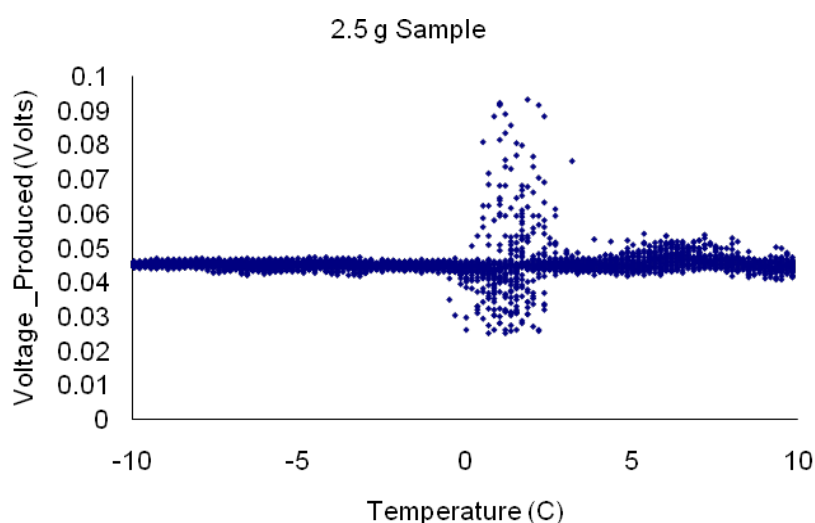
Figure 27 Voltage vs. temperature graph showing the response of the
PVDF to a 2.5 gram sample of GSG. This result is fairly typical of
most samples. Shift in the response is caused by improper contact
between the thermocouple and sample, which results in a offset of the
actual temperature of the sample.

As voltage was monitored as a function of temperature, some of the systems

experienced the pyroelectric effect as shown in Figure 28. This Figure was linear fit with

the best possible scenario.

Pryoelectric Effect in 1g GSG
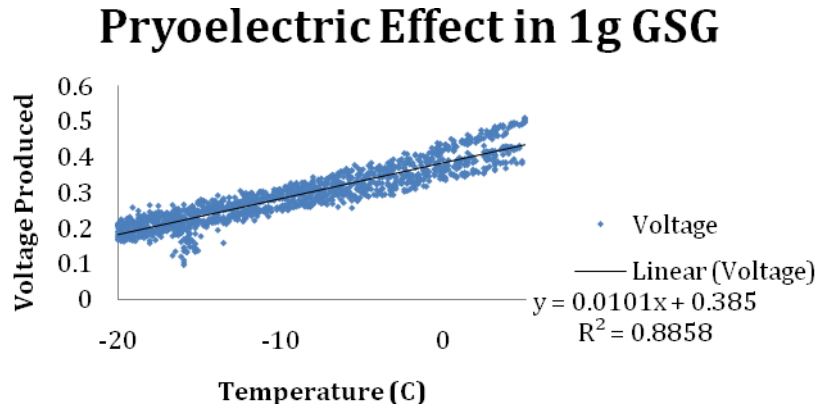
Figure 28 Temperature vs. voltage graph showing the linear nature of the PVDF pyroelectric effect over the region being studied on a one gram PVDF/GSG device. Trend-line and fitting information are shown as well.

This effect can be treated as linear and removed from the regions of interests; this is done by finding the line of best fit for the voltage versus temperature curve and subtracting that from the voltage curve. After subtracting the line of best fit, the voltage produced no longer shows the pyroelectric effect, this is shown in Figure 29.
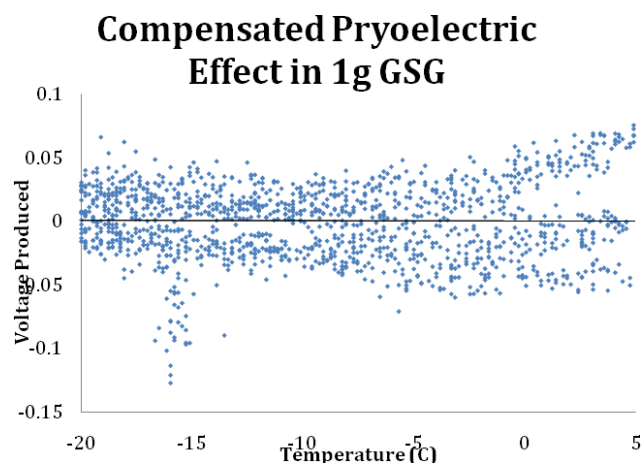
Figure 29 Temperature vs. voltage produced in the same one gram PVDF/GSG device with the linear pyroelectric effect removed. Note the similarity to the other tests without the pyroelectric effect.

It should be noted, however, that the pyroelectric effect was not present in all samples, only in the 1g system. Since this system is smaller, the PVDF is in closer contact with the dry ice, which leads to the pyroelectric effect. Once it was removed, the voltage was similar to the data produced by the rest of samples.

4.4. Crystallography and Microstructure

This section describes the different crystallographic and microstructure results collected by the different analysis techniques described in the Chapter 4. This section has two different sections, first crystallographic effects noticed by XRD. The second section describes microstructure characterization centered on the discovery and characterization of grain like features and effects of processing on these properties.

The crystallographic characterization focuses on the XRD studies and was conducted on the majority of samples produced to confirm the existence of GSG

magnetocaloric structures. Investigation into the cracking problems experienced in long

term is also studied here.

The microstructure characterization centers on certain features found on the

surface and what process steps affect those features. This section discusses the impact of

process conditions, such as the number of melt cycles, on the crystal and microstructure.

X-Ray Diffraction (XRD) was performed on numerous samples to confirm their

composition. The XRD results was shown in Figure 30 for the one gram sample, D2,

with the labeled crystal planes. The X-axis of this graph is the angle of the detector to

the sample surface, while the Y-axis shows the number of counts, which is an arbitrary

unit for intensity. The higher the peak, the more contribution from a particular crystal

plane. These peaks were identified by matching the plane spacing calculated through

Bragg's law. The plan indices were then identified through the spacing of a monoclinic

structure as described in Chapter 4.
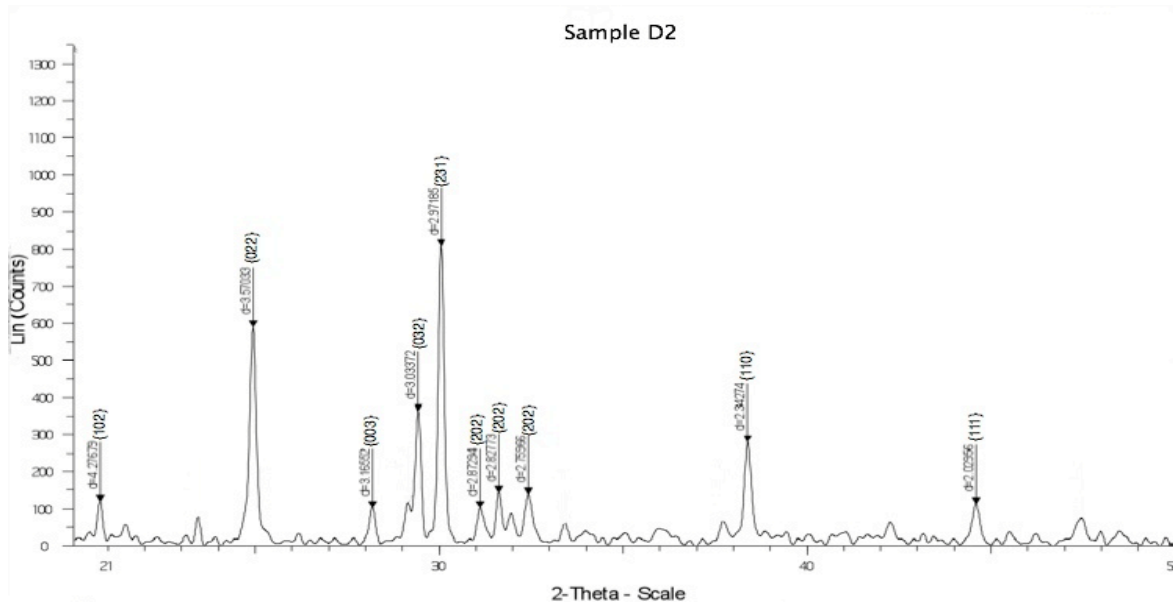
Figure 30 XRD pattern of Sample D2 showing the monoclinic structure
of Gd$_5$Si$_2$Ge$_2$. The d-spacings were calculated using Bragg's law. The
planes were identified using the standard plane spacing formula for a
monoclinic structure and matched to the d-spacings found using
Bragg's law.

The graph above clearly shows that the sample contains the major crystal planes

of a standard GSG. This confirms the existence of the Gd$_5$Si$_2$Ge$_2$ phases that are

responsible for the existence of the giant magneto-caloric effect.

4.4.1. Long Term Cracking

As mentioned in Chapter 4 section 2.1.2.1, problems with cracking of the as-cast

GSG lead to the study of the crystal structure of GSG samples after cracking occurred.

Three different sized samples were made: 1g, 2.5g, and 5g. The samples were studied

with XRD and stored until they cracked. After four weeks, four (4) samples cracked.

Figures 31 and 32 show the comparison plots of the XRD data from the before and after

XRD studies.
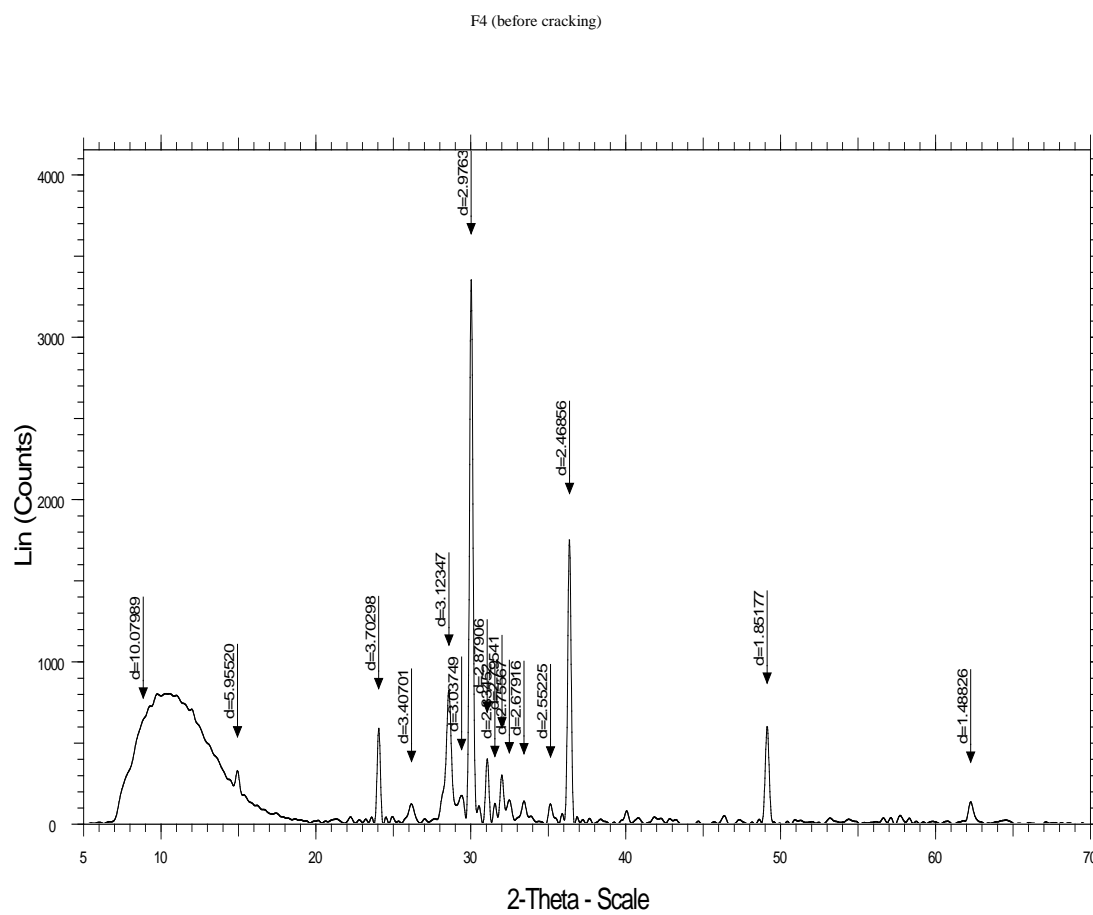
Figure 31 XRD plot showing the crystal structure of the sample before cracking occurred. This test was performed immediately after arc melting of the sample.
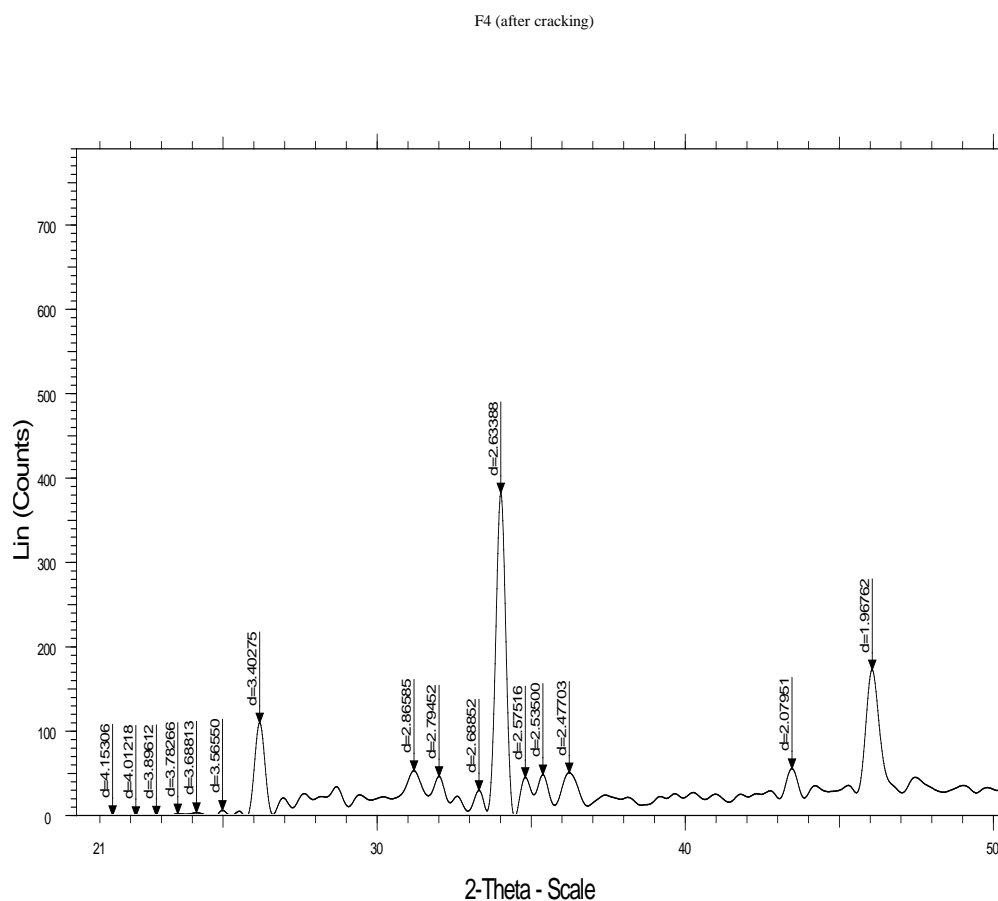
F4 (after cracking)

Figure 32 XRD plot showing the crystal structure of the same sample
as above after cracking occurred. Note the positions of the major peaks.

Figures 31 and 32 show a 5 gram sample (F4) that was tested under the exact

same conditions before and after; the only change being that the sample had cracked.

The crystallographic structure of the material has clearly changed but what change

occurred is unclear because of the lack of published information on the crystal structure

of this material. This is discussed and described in more detail in the next chapter .

4.4.2. Microstructures

4.4.2.1. AFM Study

The surface of a 1g sample, number D2, was studied using an Atomic Force Microscope (NanoR) in various locations. The AFM was run in the contact mode with a standard silicon AFM probe. First of all, a 15x15 micron scan was conducted to study the surface morphology of the sample after polishing. Shown in Figure 33 is the height image of this scan. This scan shows a characteristic area of the surface of the sample. The lighter colored features in this image mean that they are high points in the topology of the sample while the darker areas the deeper.
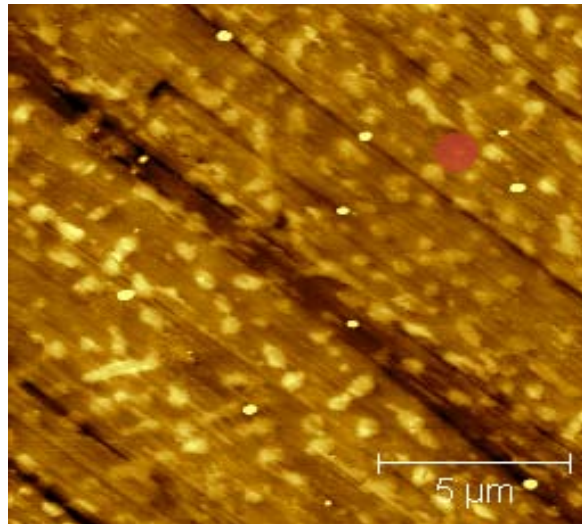
Figure 33 AFM height image of the surface of sample D2. Note the grain like structure of the higher portions of the image. The 8 highest specks are silicon carbide pieces from the polishing process.

In Figure 33, the highest features are the specks that look similar to dust on the surface. These are silicon carbide wear particles left over from the polishing process.

There are also prominent wear tracks on the surface from the polishing process. The most striking features, however, are the small grain-like spots on the surface. To investigate these features further, a smaller, higher resolution, 5x5 um area scan was conducted in the same region, The height and phase images of this are presented in Figure 34.
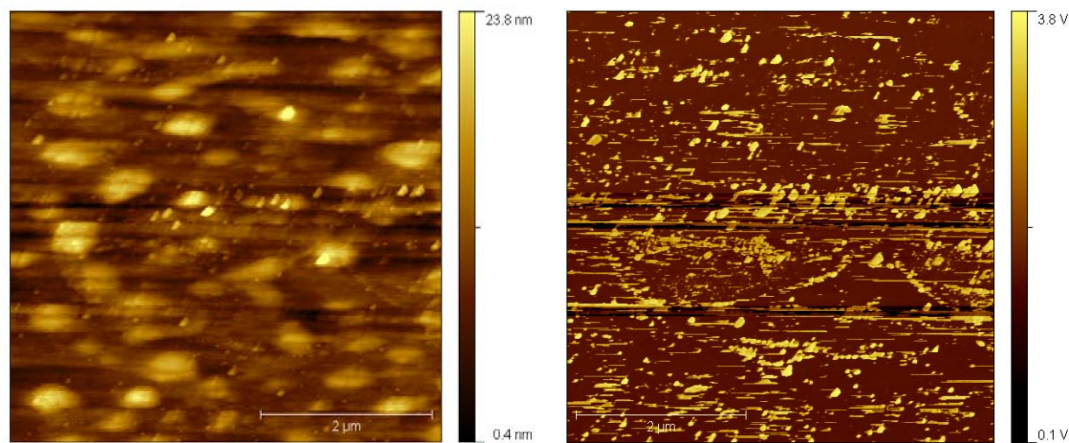
Figure 34 AFM height (left) and phase (right images) of the Sample D2. Note the position of the grain images on both the height and phase images and that the phase images don't show the same structures. This indicates that there is not a significant difference in material properties.

These features are distributed across the entire sample surface after a series of scans. Image analysis was conducted to quantify the relative amount of features as well as their sizes. Shown in Figure 57 is an image of a 30x30 um AFM height scan with the grain-like features highlighted for image analysis.

4.4.2.2. XPS Results

The XPS was conducted using both single point and area mapping techniques. The results of both of these tests are presented below.

4.4.2.2.1.   Single Point Study

XPS was used to study the chemical composition of the surface of the sample D2. The first stage study involved a single point study on the sample surface. The scanned area is about one square micron. Figure 35 is the overview scan of the elemental composition of the sample with the major peaks being marked corresponding to their element. This plot shows arbitrary intensity as a function of the binding energy.
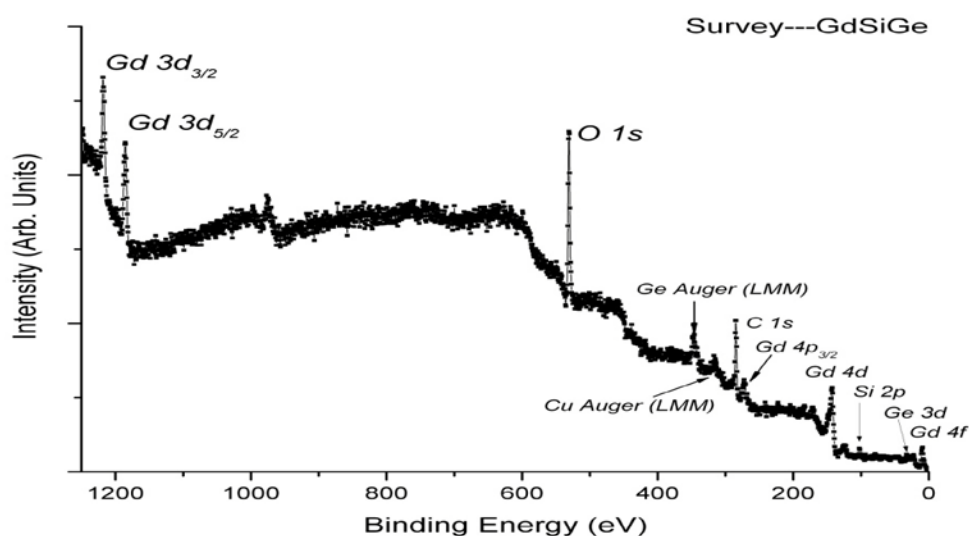
Figure 35 XPS survey scan of Sample D2 showing the contribution of the different constituent elements.

Figure 35 shows the presence of gadolinium, germanium, and silicon. In addition to the expected elements of Gd, Si, Ge , oxygen is also found. The presence of oxygen

leads to further chemical analysis by the SEM and EDS Closer inspection of the peaks

for the germanium shows an interesting feature, shown in Figure 36.
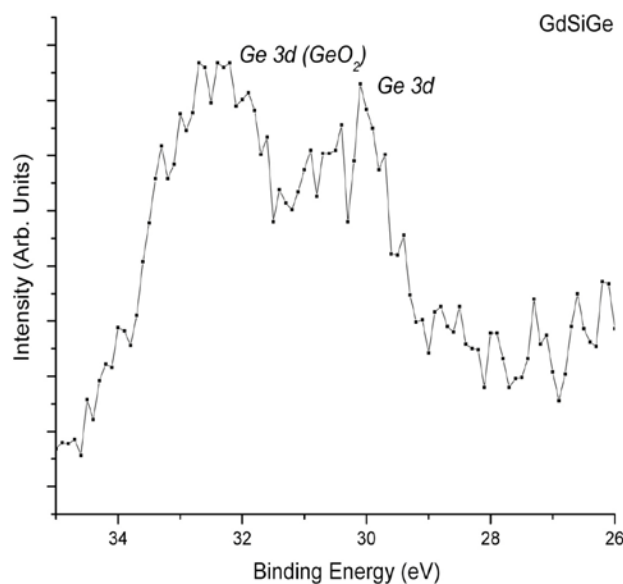
Figure 36 XPS scan of the Ge 3d peak of Sample D2. Note the doublet form of the peak indicating the presence of GeO2.

Figure 36 shows the presence of germanium, but the peak also exhibits a

shoulder similar to a double peak. This is typical of a bond that is interacting with this

electronic state. Since this is the 3d electronic state of Ge, it is likely that it is bonded to

oxygen.

The peak for the gadolinium also shows a similar feature. In this case it is the 4d

electronic state of gadolinium that shows a clear shoulder on the higher energy side of

the 4d peak. Just as with the germanium this is typical of an electronic bond, likely with

oxygen or the matrix. This graph is shown in Figure 37.
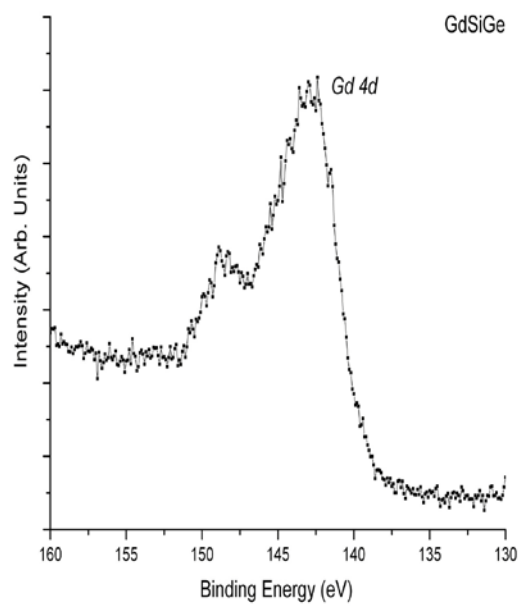
Figure 37 XPS scan of the Gd 4d peak of Sample D2. Note the
shoulder around 150 eV indicating the presence of Gd oxides.

The silicon peak is seen broaden as well. It means that the Si was oxidized to

form SiO_2. These results indicate that the elements Gd, Si and Ge are bonded to oxygen.
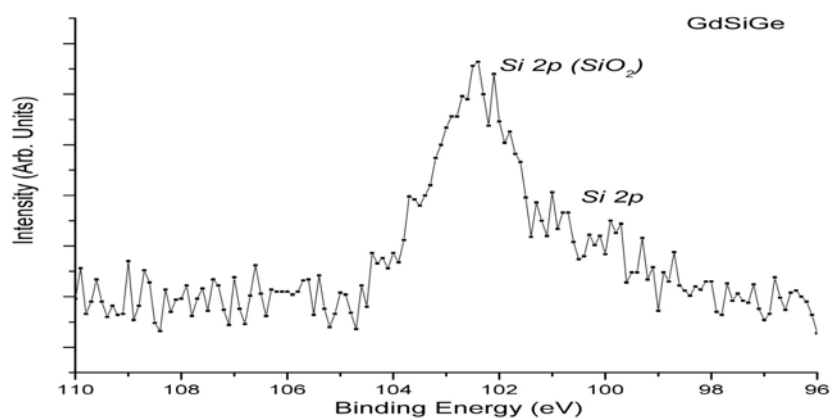
Figure 38 XPS scan of the Si 2p peak of Sample D2. Note the shoulder around 100 eV.

4.4.2.2.2.   Mapping Study

The sample was mapped using the XPS. This technique gathers mapped elements through a series of single point scans. Using imaging analysis method, elements are drawn with different grade of colors. The resolution of each pixel is no smaller than one micron. Figure 39 shows the XPS mapping scan of gadolinium. In this image, the white area indicates a high contribution of the same while black indicates less.
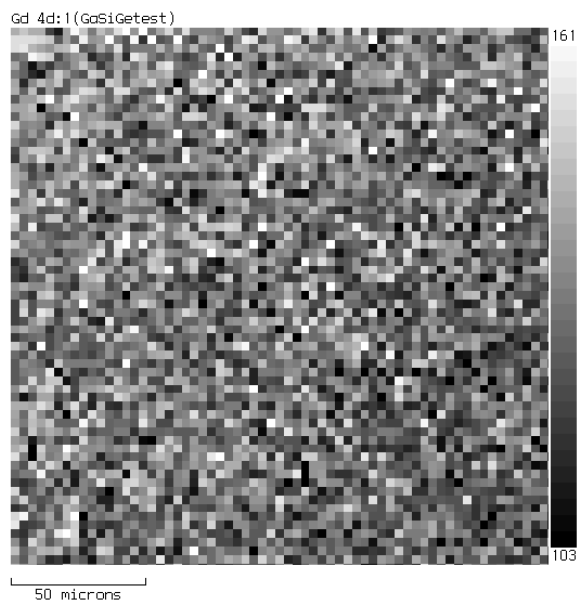
Figure 39 XPS mapping of the Gd 4d contribution on the surface of sample D2. The scan was conducted on the same region as the Ge and Si scans but at a higher resolution.

Figure 39 shows that gadolinium distributed in the area inhomogeneous. This is due to alloying. Figure 40 shows the mapping of the presence of germanium.
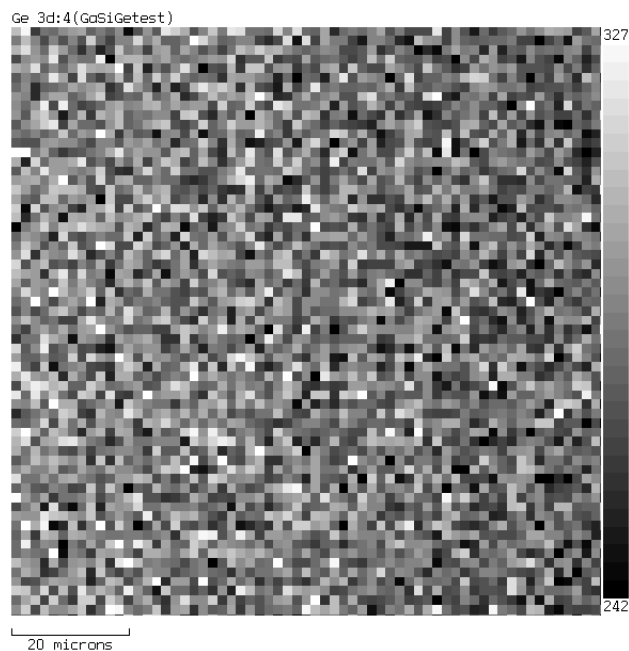
Figure 40 XPS mapping of the Ge 3d contribution on the surface of sample D2. The scan was conducted on the same region as the Gd and Si scans.

Figure 40 shows normal variations of the concentration of germanium. Similarly, the silicon distribution is shown in Figure 41.
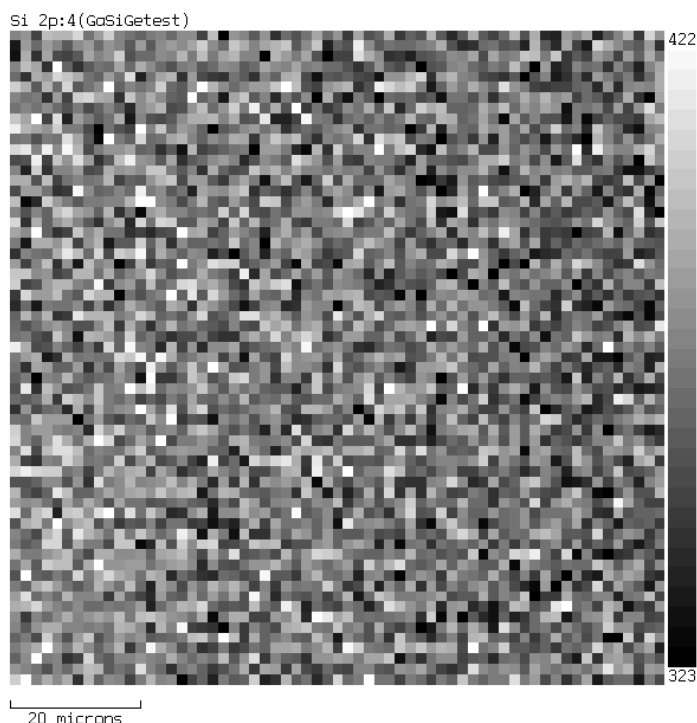
Figure 41 XPS map of the Si 2p contribution on the surface of sample D2. The scan was conducted on the same region as the Gd and Ge scans.

4.4.2.3. SEM/EDS Results

SEM studies of the surface of the sample D2 were conducted to further explore the morphology and chemical structures. A field emission SEM was used as described in Chapter 4 section 2.4.

4.4.2.3.1.　Secondary Electron Images

Images were collected in various locations to ensure that the entire surface showed similar features. Figure 42 is a survey image of the surface, which resolves the grain-like features. This Figure, as in all SEM images, shows the number of the

secondary electrons as the electron beam strikes that particular point. This image shows

the topology of the sample surface.
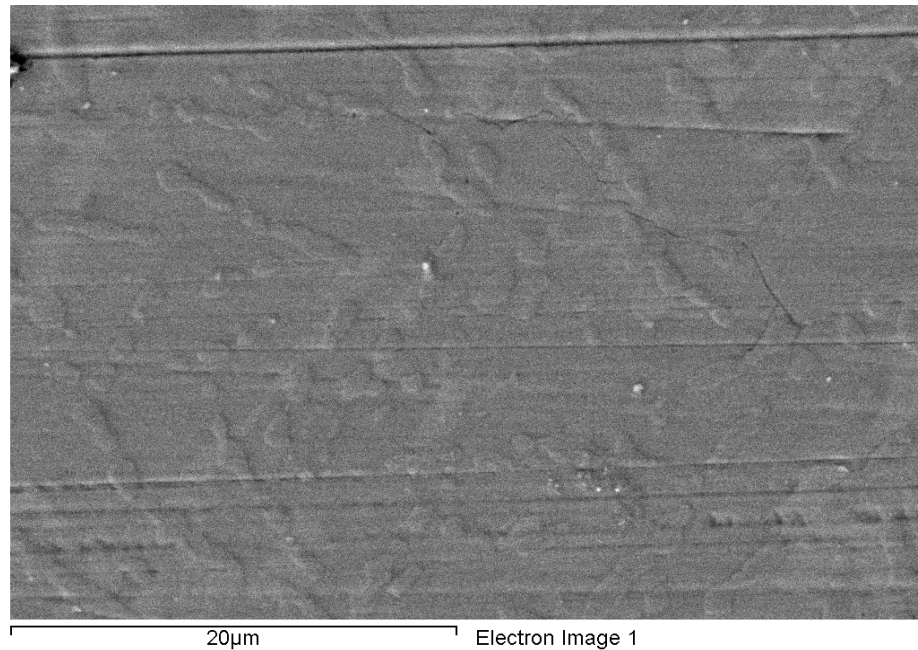
Figure 42 SEM survey scan showing the grain like structures noticed
under AFM studies. This image is of sample D2.

A higher magnification image of the same region is shown in Figure 43; it

highlights a particular grain from the survey scan.
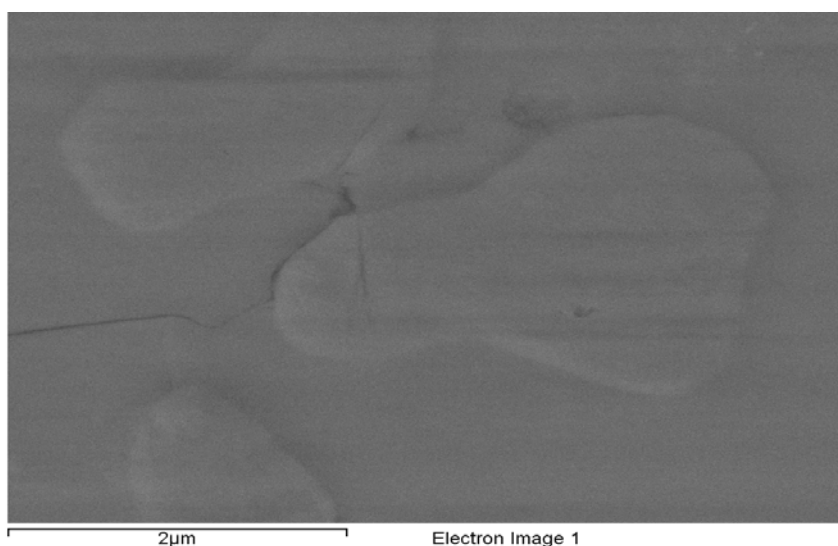
Figure 43 High magnification image of the grain in the bottom center of the image shown above. Crack in the bottom left of the image was caused by thermal expansion of the sample and should have no impact on the structure or composition of the sample or its features.

4.4.2.3.2. Energy Dispersive X-Ray Spectroscopy

EDS was preformed to identify the elemental composition of different features on the surface. The EDS allows for the data to be collected on a particular SEM image. The amount of time that the data is collected will determine the number of X-ray photons the detector receives since the number of emitted X-rays per second is relatively few. For these studies the data was collected until the resulting data image was clear and well resolved, typically about 10 minutes. Shown in Figure 44 is the EDS map for Gd, Si, Ge, O, and Cu as well as the SEM secondary electron image of the region. This image shows the mapping of the different elements.
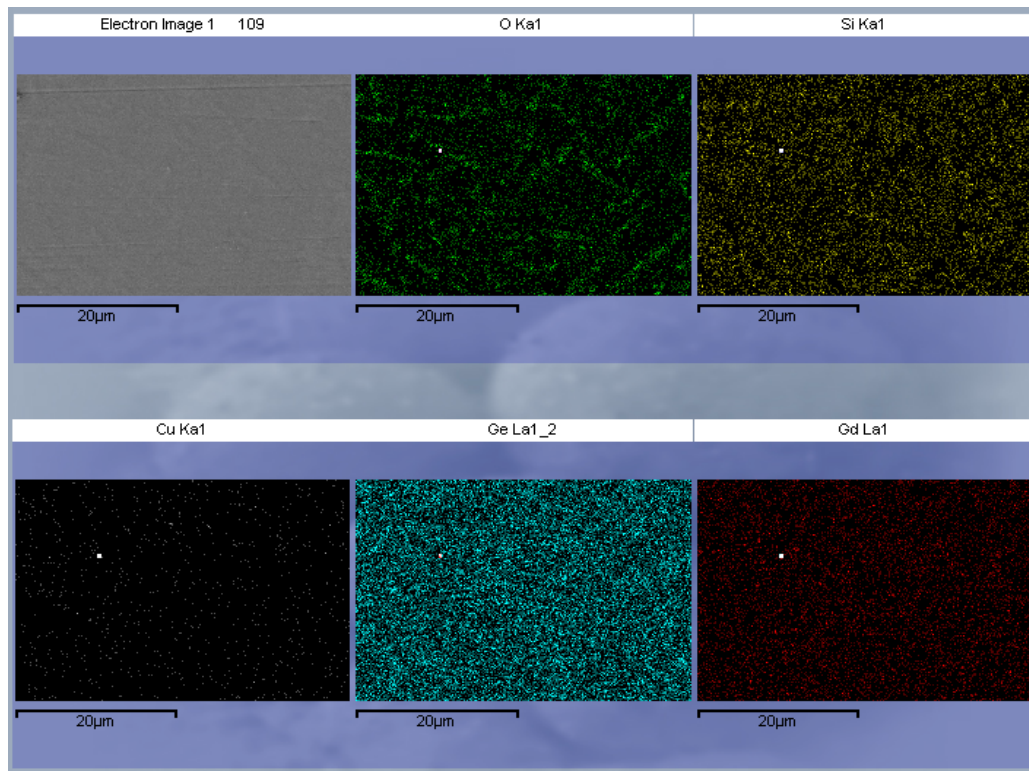
Figure 44 EDS map of the survey SEM image (shown in top left). Top center image shows the contribution of oxygen in the image. Top right shows silicon contribution, bottom left shows copper contribution, bottom center shows germanium contribution and gadolinium contribution is shown in the bottom right.

EDS maps were conducted on higher magnification region of the sample surface. They show the same sort of concentrations of materials. Shown in Figures 45 and 46 are higher magnification images of the sample showing several individual grains.
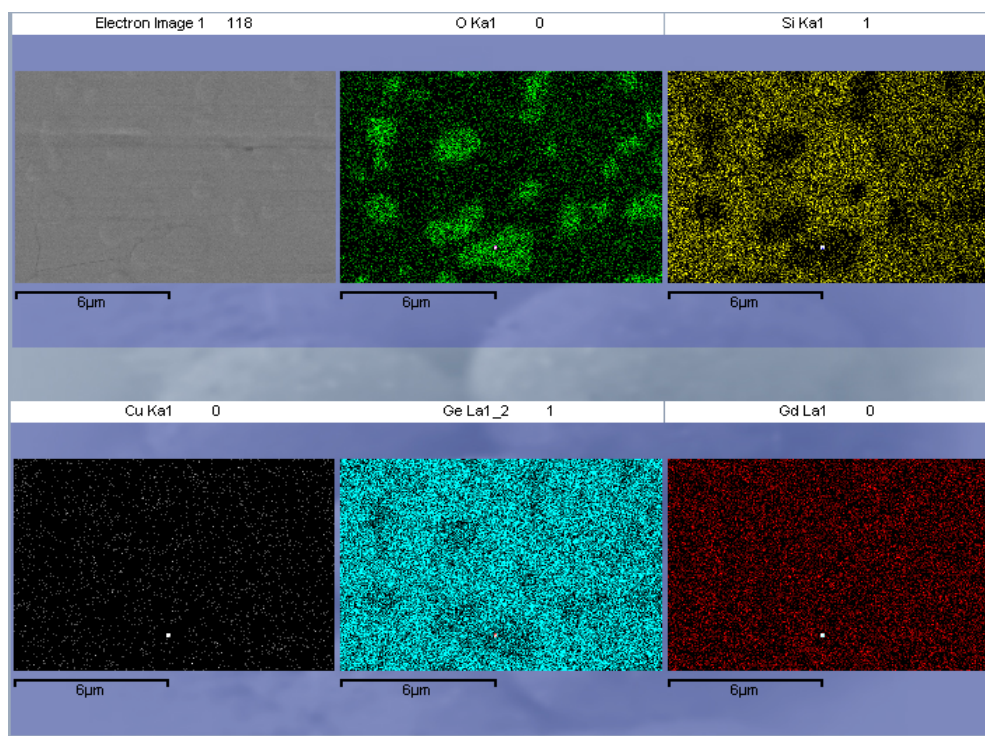
Figure 45 EDS map of the higher magnification image of the grain like structures shown in the SEM image (top right). Top center image shows the contribution of oxygen in the image. Top right shows silicon contribution, bottom left shows copper contribution, bottom center shows germanium contribution and gadolinium contribution is shown in the bottom right.
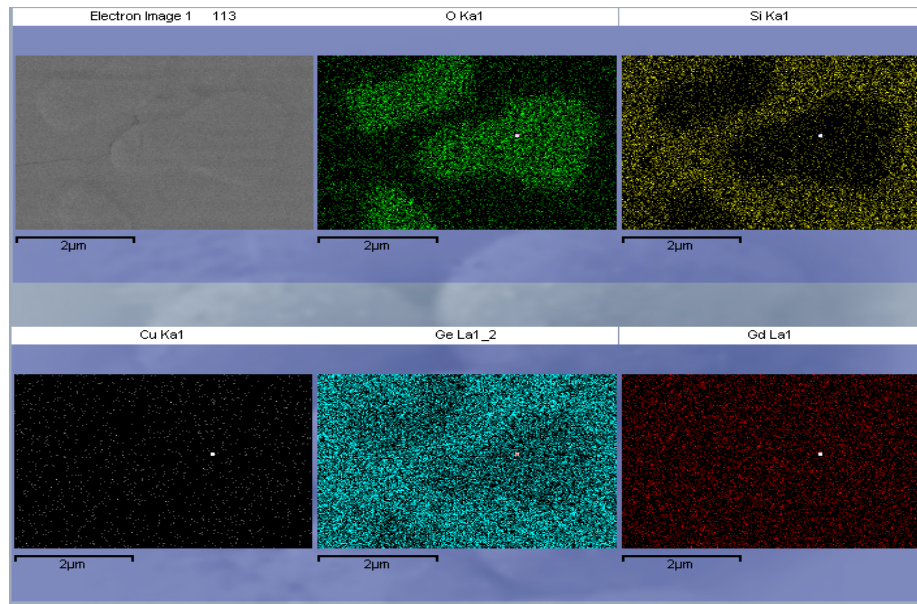
Figure 46 EDS map of the SEM image showing the single grain image (top right). Top center image shows the contribution of oxygen in the image. Top right shows silicon contribution, bottom left shows copper contribution, bottom center shows germanium contribution and gadolinium contribution is shown in the bottom right. Note that the region of higher oxygen contribution corresponds to the grain like feature almost exactly. Also note the decreased contribution of silicon and germanium.

The EDS maps show Cu in the same region as the EDS maps but it is not localized to any region. This is the predominate defect for this material. This is not surprising that it was cast in a copper crucible and may have had some copper diffuse into the sample in the form of interstitial or substitutional impurities. The concentration is extremely small. It is not expected to affect the magnetocaloric behavior, nor the structure, neither should it negatively impact the stability of the material.

4.4.2.4. Optical Microscopy

To observe the overall morphology of the same features presented above, an optical microscope was used. The sample D2 was observed with optical microscopy under a variety of magnifications. First a survey image was conducted at five hundred magnification, which is shown in Figure 47.
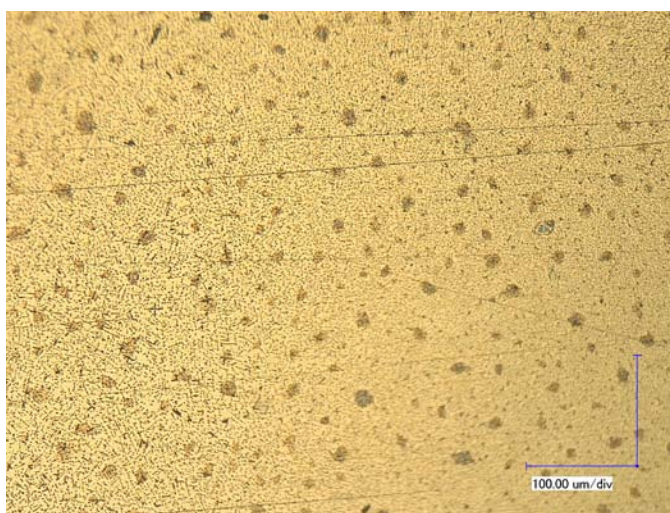
Figure 47 500x magnification survey image of the sample D2's surface. Note the very small grain features that were noticed in the AFM and SEM/EDS studies. The larger spots are caused by the degradation of the material because of crystal phase changes.

From this image two different features are visible; the first are large spots on the order of 10 microns, as well the small Figures noticed before.

The grain-like features in Figure 47 are hard to resolve at this magnification, but at higher magnifications they are clearly the same features observed before. Figure 48 is a two thousand times magnification image of these features.
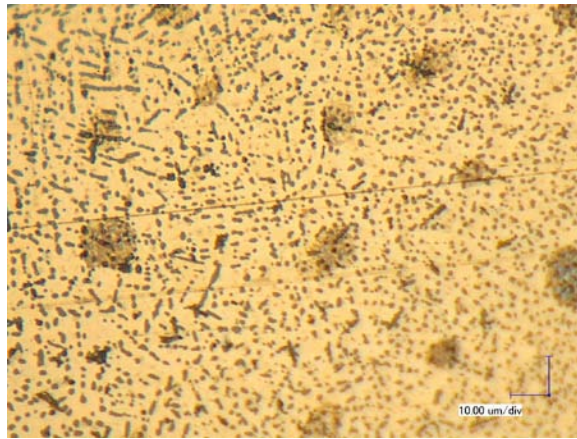
Figure 48 2000x magnification image of the sample D2's surface showing the large spots and grain like features in greater detail.

4.4.3. Effects of Melt Times

Process steps were evaluated through different melting cycles. Three samples were produced with different process times as described in the chapter 4 section 1.2.2. One sample, I1, was melted twice, the second, I2, was melted four times, and the third, I3, four times. Each sample had both XRD and optical microscopy studies conducted as well as being polished using the standard metallographic polishing process.

4.4.3.1. XRD Results

The samples that were melted a different number of times were observed under the Keyence microscope described above and studied with XRD. The XRD results, presented in Figures 49, 50 and 51, show that the structure changes with increasing melt times.

I1
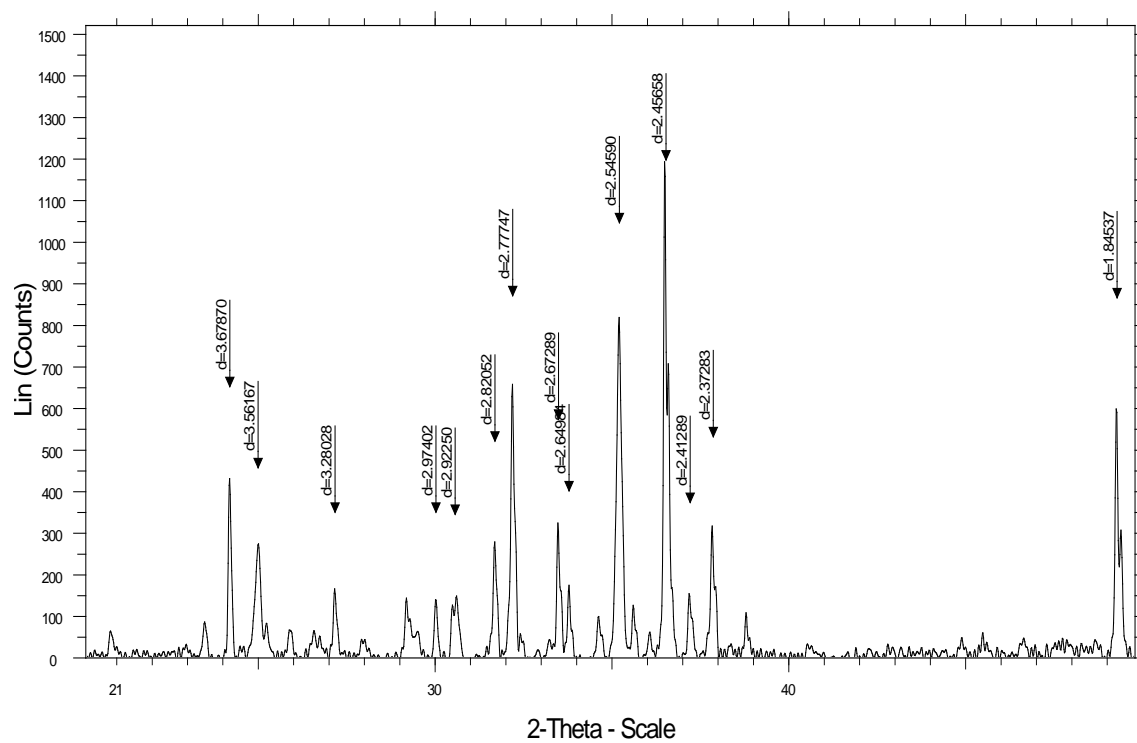
Figure 49 XRD plot of the 2 melt cycle sample.
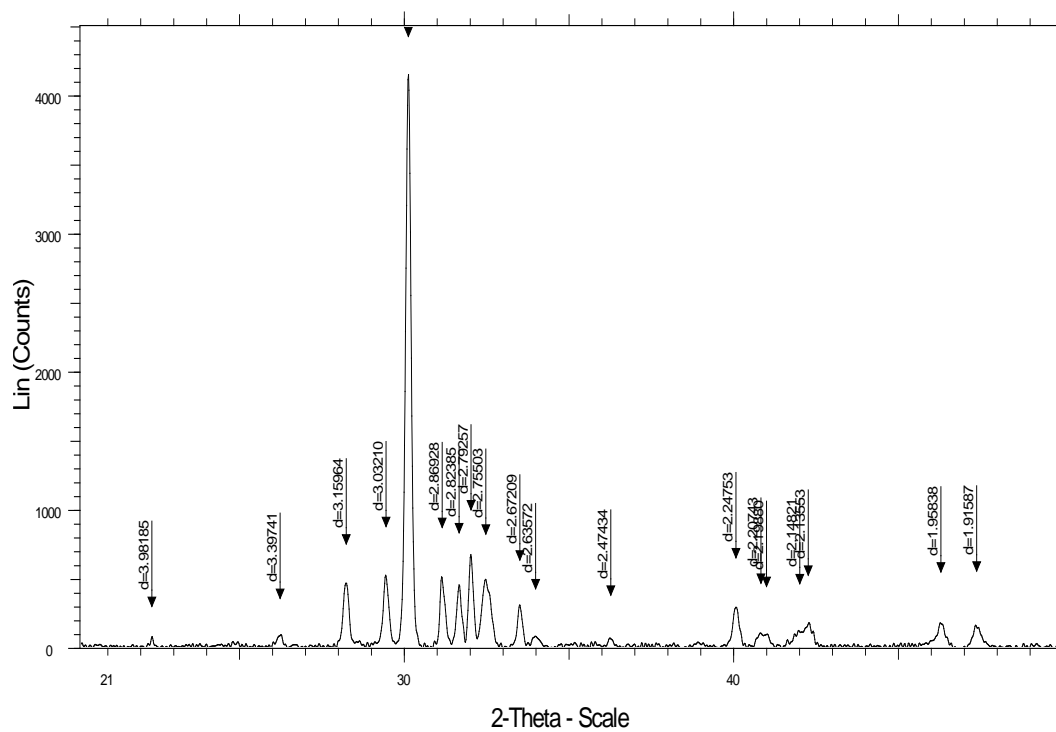
Figure 50 XRD plot of the 4 melt cycle sample.

I3
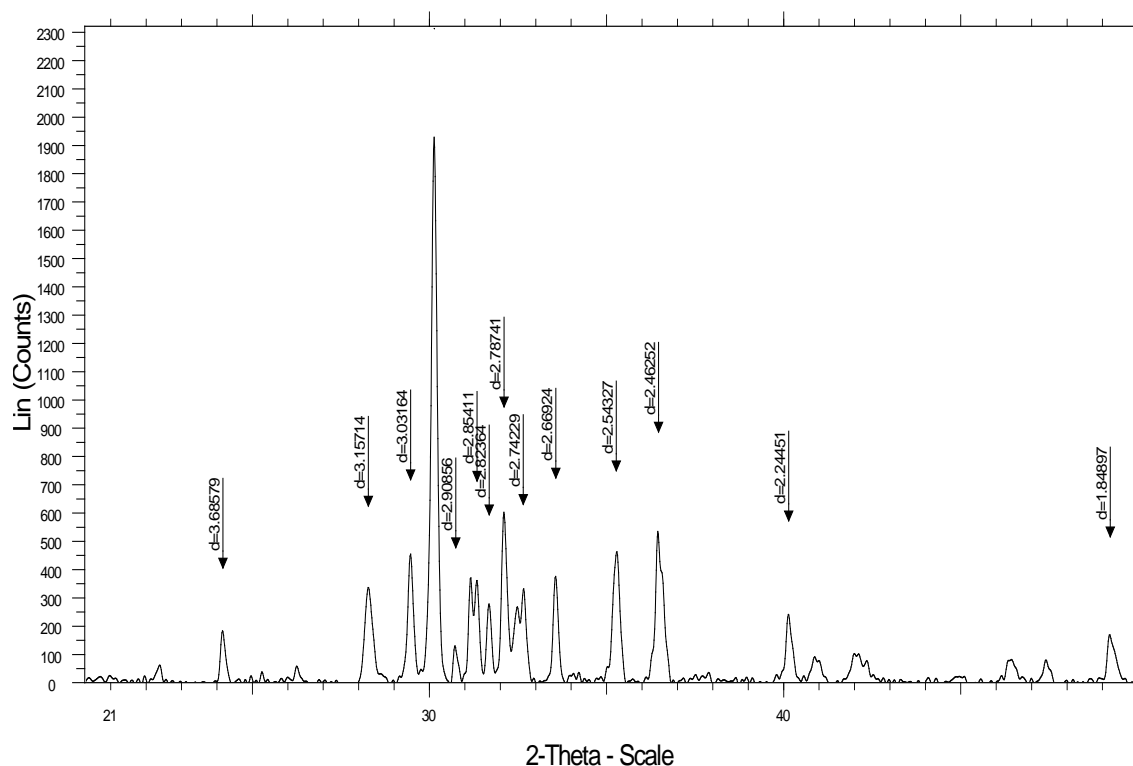
Figure 51 XRD plot of the 6 melt cycle sample.

The 49 shows the XRD structure of GSG after it was melted twice, the 50 shows

the structure of the GSG after four melts, while the 51 is that after 6 times.

4.4.3.2. Optical Microscopic Analysis

The samples were polished using the standard polishing process and were

observed under 2,000x and 5,000x magnification with the optical microscope. Figure 52

is a selection of the sample surface that is typical of the bulk material from each sample

at 2,000x.
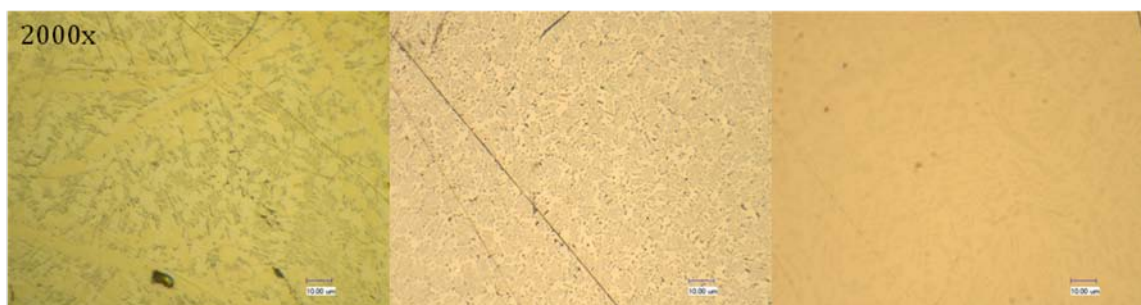
Figure 52 2000x magnification image of the sample surface of the samples arc melted different number of times. Left is the two cycle sample, center is four melt cycles and right is the 6 melt cycle sample.

The 5,000x magnification images are shown in Figure 53. These are high magnification images of the same region as those above. Note the size, shape and concentration of the small spots. It shows that with the increasing number of melt cycles the grain sizes are decreased but the number of them is increased, indicating that they are breaking into smaller structures with more melt cycles.
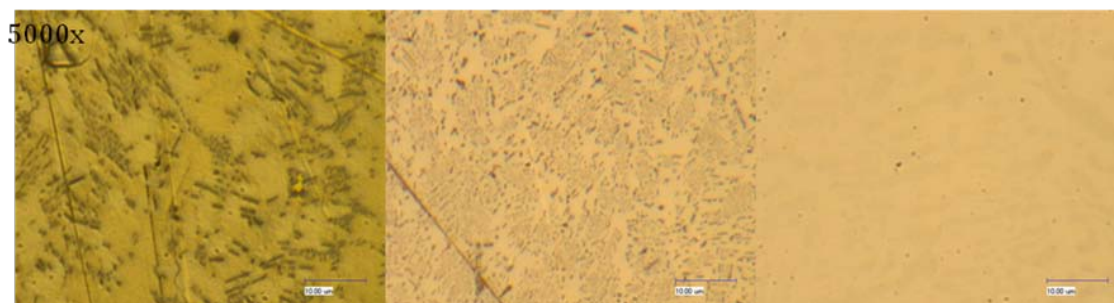
Figure 53 5000x magnification image of the different melt cycle samples. Left is the two cycle sample, center is four melt cycles and right is the 6 melt cycle sample.

CHAPTER V

DISCUSSION

As described in previous chapters, a new class of materials of multi-properties was developed. These materials can be assembled into devices for energy harvesting, thermal switching and cyclic monitoring applications. This chapter discusses the property-process of such materials and their behavior of as a laminated device. The first discusses the materials and their properties followed by a description of the performance of composite materials that use magneto caloric materials. The design, assembly, configuration, and function of devices of laminar systems is described. The chapter ends with examples of applications of such devices.

A new class of composite materials, consisting of magneto caloric and piezoelectric materials was developed in the present research. To date, there have been no reports on such materials and devices. The unique properties of such materials are discussed in the following.

5.1. Microstructure

To identify and confirm the structure of these materials, a detailed microstructure and crystallographic analysis was conducted on the as-cast GSG samples. A series surface characterization techniques were used as discussed the Chapter 3.6.

X-ray diffraction was used to analyze the crystal structures of the material. Figure 30 in Chapter 4. Figure 30 showed the presence of the monoclinic structure of GSG in the as-cast alloys. The planes are identified using Bragg's law and the atomic

plane spacing that is expected from this structure. As shown in the Figure 30, there are

the following crystal planes existed:{022}, {032}, {231}, {202}, {110} and {111}

To explore the crystal changes that occurred within the samples over time that

caused them to crack and turn into powder, XRD was preformed before and after

cracking. Figures 31 and 32 in chapter 4 show this structural change in sample F4.

Before cracking occurred the sample shows the strong monoclinic structure of the GSG

type samples (Figure 31 The structure of the material is drastically different after

cracking (Figure 32). The main features of the monoclinic GSG are typically regarded as

the peaks at and around 30 degrees in the two-theta plot. In the plot after the cracking

occurred these features are greatly decreased and the major structure is now centered at

34 degrees in the two-theta plot (Figure 32).

The analysis indicates that the new materials developed here are multi-phases,

while the structural data on these materials is limited it is likely that these phases are

Gd_5Ge_4 and $Gd_5(Si_xGe_{1-x})_4$ type structures. They potentially have multi-function that will

be discussed later in this chapter.

5.1.1. Chemical Composition

To study chemical composition, XPS analysis was conducted. Shown in Figure

54 below is the XPS spectra of the sample D2. There are several peaks labeled as Gd, Si,

Ge as well as the existence of the oxygen peaks.
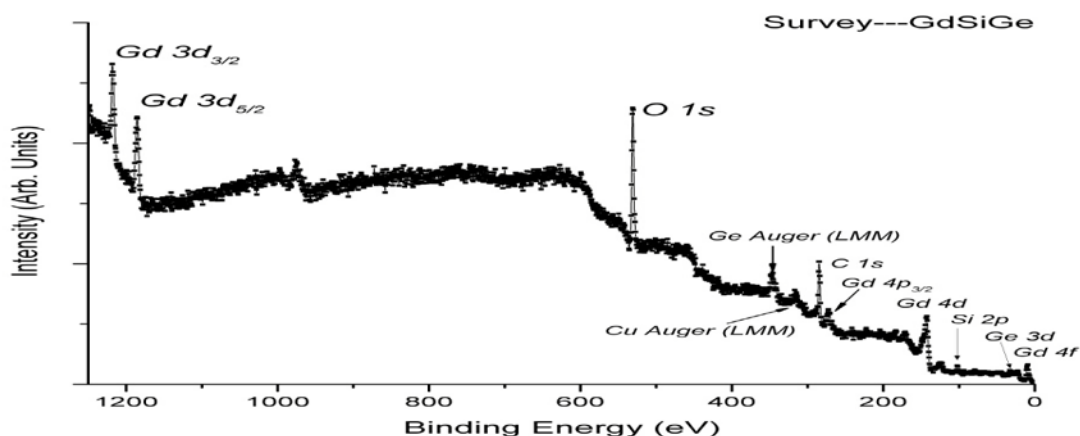
Figure 54 The XPS spectrum of Sample D2. This graph labels the
peaks with with each corresponding element.

Oxygen on the surface of the elements is common because of the oxidation

processes that occur with all materials when exposed to air. This graph and the Figures

36, 37, and 38 clearly show that there is oxygen on the sample and it is bonded to the

other elements. The initial response to this oxygen is that it is simply a oxidation coating

formed by the exposure to air. The existence of oxygen on similar materials has been

reported by Wu et. al. standout.[46]

XPS mapping was conducted on the sample at the same time as the single point

studies and it was found that there are local variations in the concentration of each

element. While this is expected from the majority of alloys, it has strong implications for

the structure of GSG type materials. GSG type materials are extremely sensitive to small

changes in the concentration of the constituent elements. The work by Kumar et al

showed that slight changes in the ratio of the Si and Ge in the compound could alter the

structure.[36] This means that the local variations of elements observed in the XPS map

could mean the phase transformation of crystal structures. The reason for this variation is inherent in the process of casting alloys. Since the pure elements are added in discrete entities (chunks or powder), their dispersion is controlled by diffusion. This is a random process and unfortunately will take an extremely long time to become completely homogenous. The arc melting process used in this research is effective at providing a minimum level of homogeneity and should not negatively impact the material. In order to confirm this, a detailed micro XRD based study should be conducted in the future to confirm that the regions of local variations are the intended composition.

Previous results have indicated that there existed high concentration of O on the surface. The surface presented with grain-like features. To understand this further, EDS analysis was carried out. Figure 55 is the image obtained using the secondary electron, similar to that shown in Figure 43.
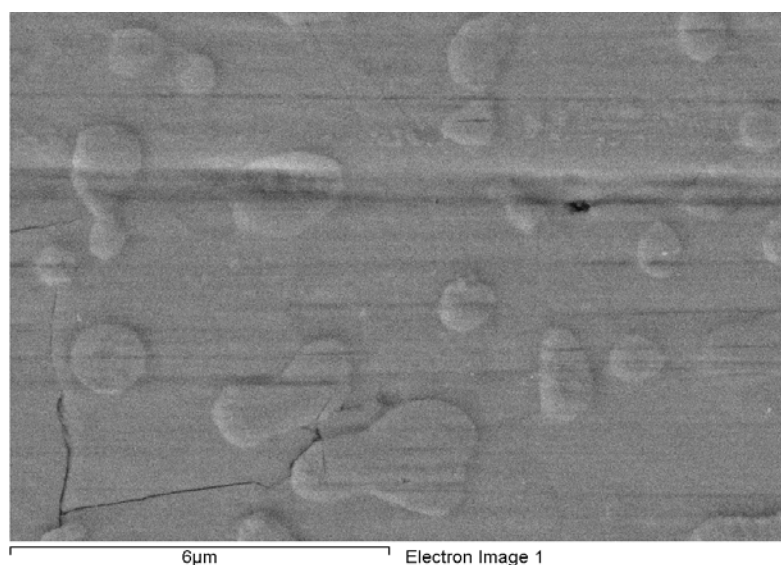
Figure 55 Secondary Electron image of the grain like structures on sample D2's surface. Crack in the bottom left of the image was caused by thermal expansion of the sample and should have no impact on the structure or composition of the sample or its features.

In Figure 56, there are six images. The Fig. 56a is the secondary electron image, 56b is the elemental mapping of oxygen, 56c is the elemental mapping of silicon, 56d is the elemental mapping of copper, 56e is the elemental mapping of germanium and 56f is the elemental mapping of gadolinium. The high intensity of the mapping shows the high concentration of the corresponding element. The Figure 56 shows strong presence of oxygen localized in the grain-like features that noticed before. Additionally, it shows a slight decrease in the contribution of Si and Ge. This decrease is caused by the fact that these elements are bonded to the oxygen present in that region and are not emitting as a strong signal. Figure 56 shows the EDS map of the region shown in the Figure above.
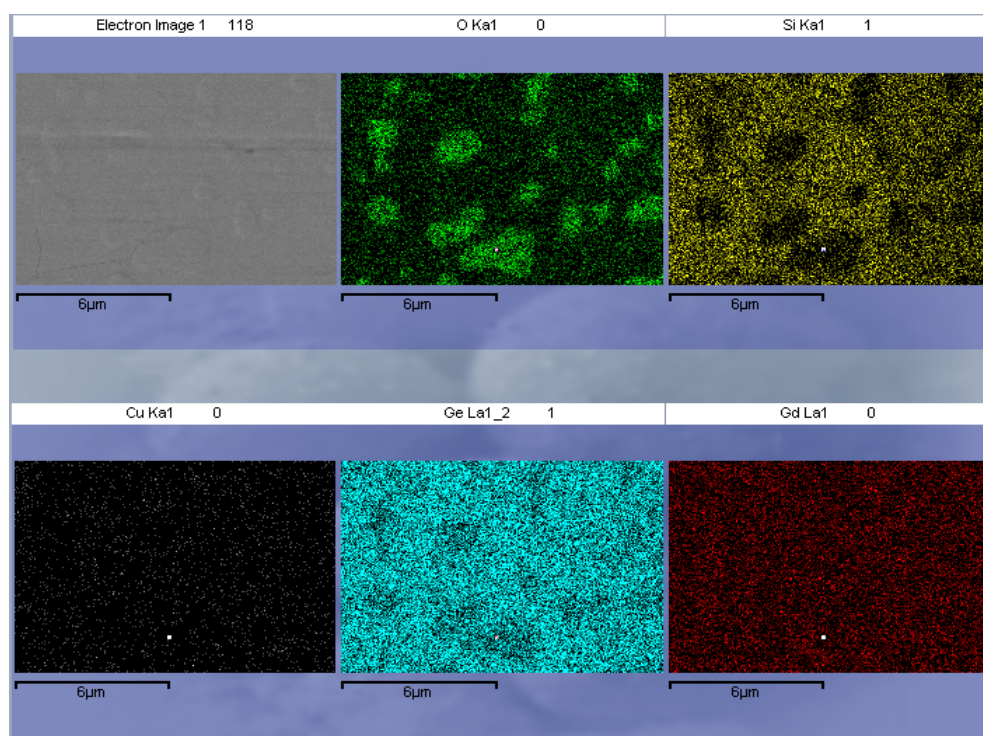
Figure 56 EDS map of the higher magnification image of the grain-like structures shown in the SEM image (top right). Top center image shows the contribution of oxygen in the image. Top right shows silicon contribution, bottom left shows copper contribution, bottom center shows germanium contribution and gadolinium contribution is shown in the bottom right.

The Figure 56 also shows that the grain-like features are also regions of higher oxygen concentration. This means that during the arc melting process oxygen built up on in these regions and stabilized the formation of the orthorhombic structure of GSG at the high temperatures in the arc-melting furnace. The reason for the stabilization has been discussed by Wu et al.[46] Under standard atmospheric conditions, GSG is a monoclinic. So from the presence of the oxygen it is believed that there is both an orthorhombic phase and a monoclinic phase.

5.1.2. Structural Distribution

To explore the crystals forming in the GSG, AFM was used for surface analysis. This technique allows for individual grains to be resolved and studied. This process shows two different phases of the material and in the form of the grain like features on the sample, as shown in Figure 57 below.
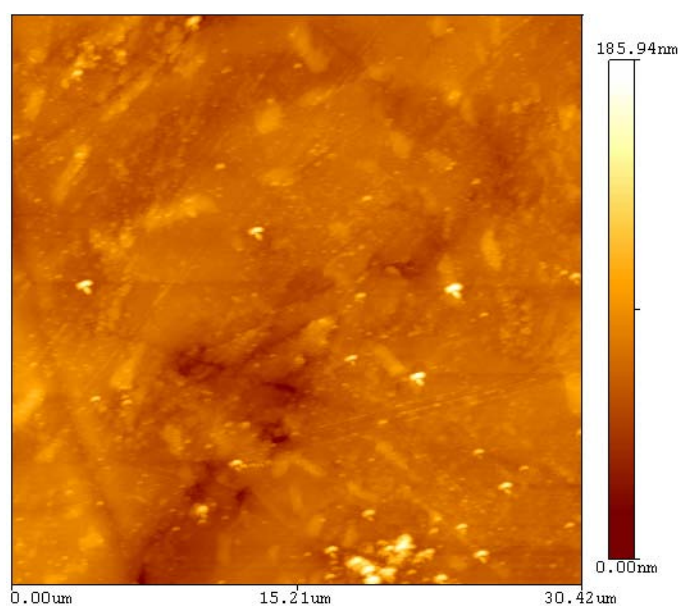
Figure 57 AFM Image of the surface of sample D2. Scan area is 30 um by 30 um.

This image shows the grain like features and in order to see the contribution of these particles, image analysis was used. The image analysis described in chapter 3 was preformed on Figure 57 shown above the results of which are shown in Table 8 below.

Table 8 Grain statistics based on the image in Figure 57.

Grain Statistics	
Number of grains	1349
Total projected area (abs.):	212 µm2
Total projected area (rel.):	23.56%
Mean grain area:	$157 \times 10\text{-}15$ m2
Mean grain size:	303 nm
Total grain volume (zero):	1.53 µm3
Total grain volume (minimum):	1.20 µm3

This table shows that the average grains are approximately one third of a micron long and occupied roughly a quarter of the sample surface.

To explore the contribution of the orthorhombic phase in more detail by observing larger areas than the AFM studies and to test the viability of lower cost techniques optical microscopy was used. Magnified images as low as 500x like Figure 47 in chapter 5 show that this technique is sufficient to resolve these features. More detailed images and analysis show that the orthorhombic phases are able to be resolved with optical microscopy.

The 500x magnification images show the presence of large features on the sample surface. These images were taken several weeks later and the sample was starting to crack. Higher magnification images of these large features show these features as encompass the orthorhombic grains in the sample. Table 9 shows the amount of area that these features occupy in Figure 47.

Table 9 Table showing the amount of area that the large spots contribute to the area of the samples. Data was collected from the image analysis program ImageJ.

Large Pixel Area Percentage	
Data Number	Large Spot Pixel Area
1	18833
2	4528
3	8690
4	6693
5	10101
6	3072
7	12239
8	14969
9	6804
10	16944
11	6702
12	8331
13	4848
Total	122754
Image Area	1917201
Percent Area	6.40%

Pecharsky et al. explained the nature of the crystal structure under different cooling rates which provided an explanation for the cracking.[40] Rapid cooling, as occurs during the melting process of these materials, creates a metastable phase of the material.

This metastable phase can then decay which causes the cracking in the samples. These large features are the sites were this metastable-to-stable transformation occurs causing the cracking. Sample D2 in this study developed serious cracking problems several weeks after the the optical microscopy was conducted, which seems to confirm this.

To study the amount of the orthohrombic grains in the sample, more optical microscopy image anylsis was studied.. The image analysis was conducted on all of the optical microscopy images taken and compiled in to the table as listed in table .

Table 10 Table showing the contribution of both the large and small features to the area of sample D2's surface.

Grain Structure Area Percentages		
Magnification	Spot Area %	Other Area %
500x	37.45	62.55
1000x	30.29	69.71
2000x	32.1	68.8
5000x	38.43	61.57
Average	34.45	65.55

The orthohombic phase accounts for 34.45% of the sample while the monoclinic struture accounts for the other 65.55%. This agrees with the results from the AFM image analysis.

5.1.3. Process-Property Relationships

In order to study effects of melting times on the monoclinic and orthorhombic grain structures, the melt cycles were evaluated. Both XRD and optical microscopy were conducted on the samples that were melted for 2, 4, and 6 times.

The XRD spectra are shown in Figures 49, 50, and 51 in chapter 5. The XRD pattern for the 2-melt sample shows a rough and poorly defined structure with a large number of different crystal planes. The normal peaks that are associated with GSG (around 30 degrees) are weak in comparison to the rest of the peaks. This indicates that the GSG structure has not fully formed and is a poor representation of GSG type materials.

The XRD pattern for the 4-melt sample (Figure 50) shows an improved structure that is very characteristic of GSG. This indicates that magnetic crystalline structures of GSG were clearly formed and dominated in this sample. This process was considered close to be optimized and had been used for other samples in this research.

The pattern of the 6-melt sample, in Figure 51, shows an even further reduction in the minor peaks of the structure but still retains the magnetic characteristic features of GSG. The sample containing the main features around 30 degrees are present but the other features are removed.

The optical microscopy studies show a change in the microstructure of the orthorhombic structures depending on the number of melt cycles. Image analysis was done on the Figure 52 in chapter 4 and the results are present in table 11 below. The 2-melt cycle sample shows a large number of these features, while the 4-melt time sample shows a reduction in the size and contribution of these features. In the 6-melt time sample these features are completely removed. In addition to the change in the number of the particles the size is different as well. Figure 42 in chapter 4 shows that the 4-melt time sample has smaller and more uniform in shape than those in the 2-melt time sample. The 2-melt time sample has two different shapes of grains. The first are small

circular grains, while the second are longer rod-like structures that vary in length greatly.

This could be from randomly oriented cylindrical grains that are being viewed at

different angles causing them to appear to have different size and shape. This is

supported by the large deviation in the size of the particles in the 2-melt time sample.

The features registered by the image analysis in the 6-melt time sample are aberrations

caused by dust trapped in the optical path of the microscope and should be disregarded.

Table 11 Statistical analysis of melted samples.

Melt Times	Grain Count	Average Particle Size(um)	Standard Deviation (um)	Area Percent
2	395	1.26	3.654	18.3
4	3099	0.138	0.297	15.5
6	10	0.205	0.251	0.1

This shows that the increasing number of melt cycles reduces the amount of the

orthorhombic grains significantly both in size and area percent. The increased melting

times decreases the amount of the orthorhombic phases. This indicates that the

orthorhombic phases formed earlier in the synthesis of the material but the exact process

leading to their formation is not known. It appears that the increasing melting cycles

reduces the orthorhombic phases. The reason for this is not exactly clear and should be the subject of further investigation.

5.2. Multifunctional Composites

As described in the previous chapter, a class of composite materials with dual active properties was developed. These materials are a PVDF matrix with GSG as a filler material. The aim was to combine the piezoelectric properties and the large thermal expansion properties of these two materials. This goal was successfully accomplished and was the first of its kind combing such properties.

5.2.1. GSG/PVDF Piezoelectricity

The piezoelectricity is response of such a material to a force/strain or a field of electricity. When combing the magnetocaloric GSG with the PVDF, it is expected that the internal strain induced by the GSG affecting the matrix. Indeed, this was found in the Figure 19 in chapter 5 where a high voltage produced by the material when compressed. This confirms the presence of the piezoelectric property of this composite. As noticed that the testing conditions were not optimized.

5.2.2. Composites

The function of these materials takes advantage of PVDF's piezoelectric microstructure and the fact that the inclusion is bonded well with the matrix. As the GSG inclusions expand inside the PVDF, they exert a strain and corresponding stress in the same. When the PVDF experiences these forces it produces an electric field in the material. This is the mechanism behind the functioning of this composite material.

It was interesting to note that although the particles of GSG was randomly distributed in the matrix, their expansion due to temperature change had significant net

increase in the output voltage. This was shown in the Figure 22 of chapter 5. The reason

that this net volume change was not canceled is because of PVDF's preferential

actuation in the 31 direction. It has been reported that the piezoelectric polymer

underwent phase transformations, particularly ß to γ.[17] When GSG was added to the

matrix, the local expansion enhanced stretching of polymer molecules, i.e., the phase

transformation. As a result, a higher output is obtained.

The graphs of the voltage response for all of the GSG materials show a strong

response in the region of the transition temperature of GSG, as shown in Figures 22, 23,

24 and 25. The temperature changes are due to thermal transfer between the

thermocouple and the material. This does not detract from the fact that these composite

films are responding to the phase transformation of the GSG and producing a net output

voltage.

The power produced by each sample per area was calculated and is shown in

Figure 58 as a function of concentrations (wt%) of GSG. The power was calculated

using the sum of the voltage produced by the system as it was cooled with dry ice. These

values are the average of three different samples over three different tests each and the

standard error for each is labeled.
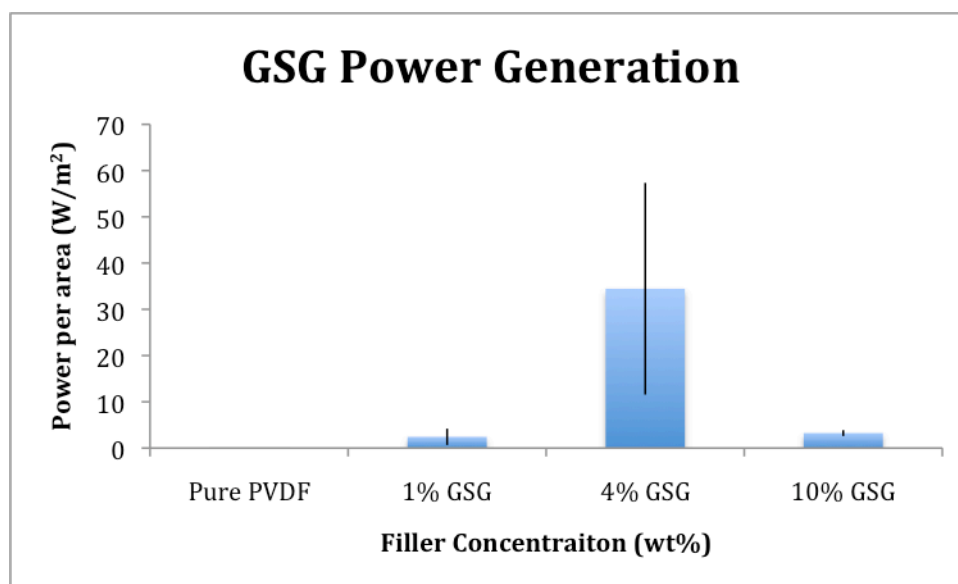
Figure 58 Chart showing the average power of the different powers produced by the different weight percentages of GSG. Error bars show the standard error of the entirety of the samples tested.

As seen in the Figure, the GSG based composites produced a strong power upon actuation of the GSG. The 4% GSG composite produced the largest amount of power with 34.5 W/m^2. The 1%wt and 10 %wt composites produced 2.4 and 3.2 W/m^2 respectively. All of these values are significantly higher than that of the ZnO (discussed later) based composites when considering statistical variations. The 4% GSG material stands out among the GSG based composites. This means that there is an optimal concentration where the internal expansion by GSG enhances the phase transformation of the piezopolymer.

While these three studies show that there is an ideal concentration of particles, they do not show the effect of particle size. This research shows that this type of material is feasible and could have a variety of important applications, particularly that of energy

harvesting in situations with rapid thermal cycles. There needs to be a detailed

microstructure based study into the effect of the GSG filler on the PVDF matrix.

To eliminate the potential phase transformation of PVDF induced by temperature

change, the ZnO composites were synthesized and tested for power output in the exact

same procedure as the GSG-PVDF material. Results are shown in the Figure 59 below.
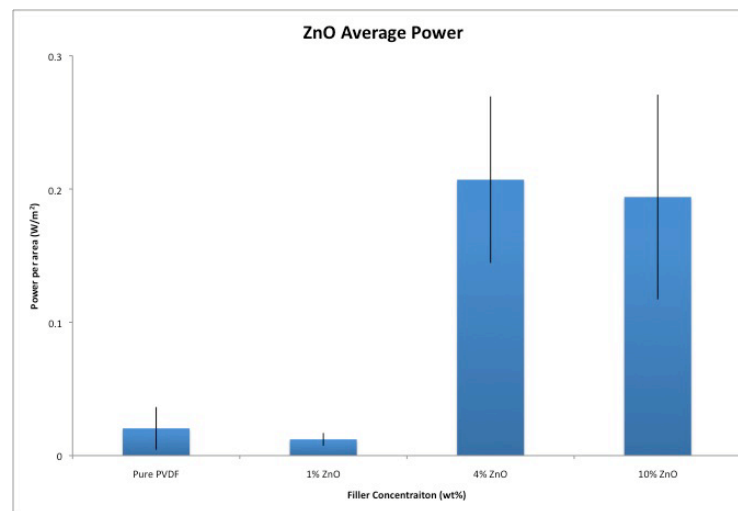
Figure 59 Chart showing the average power of the different average
powers produced by the different weight percentages of ZnO. Error
bars show the standard error of the entirety of the samples tested.

The ZnO is a piezoceramic material. The composite made with ZnO as a filler

did not produce a voltage spike like the GSG composites. This means that the PVDF

does not have a phase transformation at –4 ^{o}C. The ZnO based sample generated a very

small amount of power due to added piezoelectricity of ZnO. The highest average power

produced by these control materials was 0.2 W/m^2 by the 4%wt ZnO samples. This

amount of power is extremely small in comparison to the GSG composites. The 4 and

10%wt ZnO tests fall within statistical variation and produce a constant amount of power. The 1%wt ZnO samples produce less power might be due to the weakened matrix material.

This research has introduced a new class of material that capitalizes on the properties of two different active components. It has shown that piezoelectric composite materials using magnetocaloric fillers are not only possible but react strongly to environmental changes.

5.3. Laminated Devices

The device design was based on four different approaches targeting specific factors in order to optimize the power output. The following discusses the factors considered for each type of sensor design.

5.3.1. Effects of Geometry

The first design focuses on the geometry. This system was described in chapter 3 subsection 3.3.2.1. The first and most important aspect of the design of this system is geometry because of its impact on the efficiency and performance of the system. In this system the amount of contact between the PVDF and the GSG should be considered. This amount of contact depends on the sample, PVDF and lead placement as well as the overall contact area.

The performance of this type of system relies on the contact area of the GSG material and the PVDF (this is why the composites are so effective). This design places the sample at an angle to the PVDF surface because of the lead placement and requires that the adhesive transfer the strain from the GSG to the PVDF. This geometric problem results in decreased performance and rapid breakdown of the device. From this system it

is clear that any future system should be designed to maximize the area of contact between the GSG and PVDF.

This design revealed that a flat contact is recommended for both the GSG and PVDF unless a more effective geometry can be made. To further improve the contact, surface texturing could be an alternative such that to increase the real contact area between GSG and PVDF. This would allow the surface areas of the samples to be increased causing an increased real contact area. Until the material processing conditions allow for these improvements a flat contact geometry should be used.

5.3.2. Interfacial Bonding

Interfacial bonding deals with the bonding strength between GSG and PVDF sheets. The device described in chapter 3 subsection 3.3.2.2addresses the importance of good interfacial bonding through adhesives. The stability of the adhesive over the conditions being studied is of great importance. This device is subjected to temperatures as low as -170 Celsius and strains of 1%, all adhesives must be able to withstand these conditions while still providing good interfacial bonding.

The adhesive originally used in this work was cyanoacrylate. It was found however that this adhesive is temperature sensitive under the region being studied. It was found that at low temperatures it would become brittle and break under the applied strain from the GSG. In order to improve the function of the system M-Bond, a commercially available solvent thinned epoxy, was used. Under the curing conditions used M-Bond can withstand temperature ranges from -270 to 50 Celsius and 1% strain.

In the future the adhesive used should be carefully considered so that the full performance of the device can be obtained. Depending on the exact design requirements

and the application of the device different conditions should be considered when choosing an adhesive. The adhesive should at least have a usable temperature range exceeding that of the device and a strain of no less than 1%. For the standard purposes of this device the M-Bond adhesive is more than sufficient.

5.3.3. Effects of Capacitor Geometry

The third design of the system points out the need for considering the capacitor geometry when designing this type of sensor. The design of the device is described in chapter 3 subsection 3.3.2.3. This system functioned admirably for approximately 10 to 15 cycles. In order to improve the lifetime and reduce the complexity of the system the silver layer on the PVDF was removed. In typical piezopolymer films a thin layer of metal is used to detect the electric field produced by the piezoelectric effect. In this system the GSG is attached to a silver layer and the repeated strain causes the interface between the silver and the PVDF to weaken and detach.

This points out a novel way of redesigning the device. The silver is an unnecessary element and its removal from one side of the system allowed the strain to be transferred directly from the GSG to the PVDF through the adhesive and not be damped by the silver layer. The GSG serves as the plate of the capacitor for detecting the electric field and eliminates another step in the system. This redesign allows for longer lifespans to be achieved resulting in a more reliable system.

5.3.4. Integrated System

The final design takes advantages of the enhancements in geometry and adhesives. Detailed description was provided in Figure 13 in Chapter 3. This system is able to perform repeated cycles without any noticeable degradation. One particular

device has been tested in excess of 100 cycles cooling cycles using liquid nitrogen and dry ice and has shown no structural degradation. It is expected that this system will be able to cycle with a magnetic refrigerator for thousands of cycles.

Future improvements of this system are relatively limited but should focus on the particular applications that are intended. For example, in situations were higher voltage signals are required, an increased contact area should be used. The adhesive selected should meet the minimum requirements for this device as far as temperature range and strain.

This development has shown the process for creating and optimizing a piezoelectric polymer based magneto-caloric monitoring system. This is the first of its kind and could have a wide variety of applications in the field of sensing and system monitoring. This proves the concept and provides a system that functions similarly to the composite based material but it allows the advantage of being mounted directly on the magnetic cooling material. This would allow for more accurate monitoring because it does not rely on a separate system for the detection of the phase change of the GSG. This system could be adhered to the GSG material and function based on the GSG's actions not on the actions of a separate system.

5.3.5. System Ranking

Each of these systems points out an aspect of the design process and should be considered in its own right. Table 12 below shows the advantages and disadvantages as well as the design aspect that this system illustrates.

Table 12 Device ranking.

Device Design	Advantages	Disadvantages	Design Aspect
Leads attached to PVDF	-Improved Voltage production -Multiple use cycles (2-3)	-Ineffective adhesive bonding -Short lifetime	-adhesive importance
Use of M-Bond adhesives	-Improved Voltage production -Improved use cycles (10+)	-Inefficient use of capacitor plates -Long production time -Less than ideal lifetime	-capacitor Plate use
Use of GSG sample as capacitor plate	-Good Voltage production -Lifespan -Reliable -Consistent	-Long production time	-Standard Design

5.3.6. Power Generation

The last design of the device was compared with a device made with a steel sample in terms of power generation. The device functions similarly to the composite material but the applications and power produced are different. As mentioned before this system would function well as a thermal switch or cyclic monitoring system when a thermo magnetic sensor is needed. Three devices was tested under the same conditions, 1g GSG, 2.5g GSG and steel based systems were all tested for the power production.

Figure 60 below shows the power produced by the different systems. The 1g system produced approximately 0.001 Watts of power during a single transition of the GSG. The 2.5g sample produced significantly less power despite having a larger contact

area. The reasons for this are not readily apparent and should be the subject of further investigation. Microanalysis on these devices should be conducted to study the interfacial properties so that they can be further optimized.
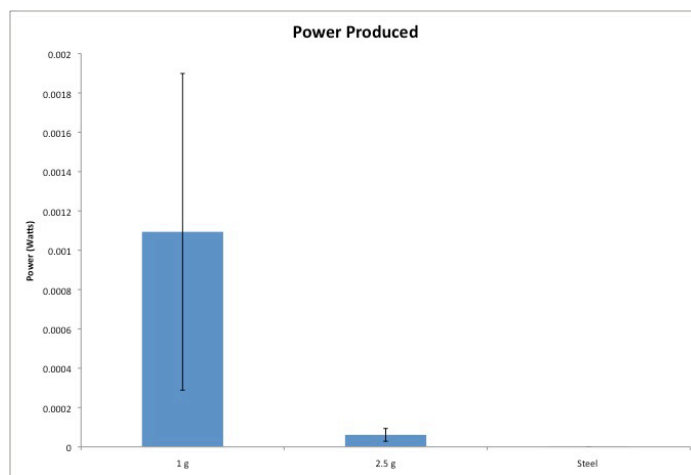
Figure 60 Power produced in watts by the different PVDF/GSG systems. Error bars show the standard error for all of the runs conducted on these systems.

The steel system served as a reference sample. The reason the steel sample was used was to be able to test effects of geometry on the PVDF resulting voltage generation. Steel was used because of its lack of thermal expansion changes in the region being studied as well as its ability to be cast into the necessary shape. As shown in the Figure 60, the steel sample produced an extremely small power and no peak characteristic of a phase transformation. The power produced was $5.13*10^{-9}$ Watts.

The design and power generation are proven to be superior and efficient. It's the first of their kind using active materials to promote power generation. This could have a significant impact on monitoring magnetocaloric materials in the future. The power from these devices is significantly smaller than that of the composite materials but these devices serve a different role as a sensor for magnetocaloric refrigerants instead of an energy harvesting system.

CHAPTER VI

CONCLUSIONS AND FUTURE RECOMMENDATIONS

This thesis research developed and characterized a new class of composite materials, and laminated devices using magnetocaloric materials. Experimental approaches were used to study the process, microstructure, and properties of the same. A prototype device was developed using such materials that have multi-properties and functions. The major achievements and new understanding obtained in this research is highlighted in the following.

- A process to synthesize magnetocaloric, piezoelectric composite materials, and laminated devices was developed. The process was optimized with the conditions with 4 to 6 melting times, at temperature of 2000 ^{o}C, and for 45 second individual melt cycles

- This research has proven the viability of measuring the phase change of the magnetocaloric material by monitoring its 1% volume change with piezoelectric polymers.

- XRD and SEM/EDS analysis showed that the magnetocaloric material had orthorhombic grains caused by oxygen stabilized phases during melting. These phases are not expected to be magnetocaloric and should be removed when possible.

- These grains can be removed and reduced by increasing the number of melting times in the arc melting process, therefore improving the quality of the material.

- Piezoelectric composites were developed that produced significant amounts of

power due to the large thermal expansion of the magnetocaloric material at the

temperature -4 C. The composite material could produce a power as high as 34.5

Watts/m^2 that was 1,725.times higher than PVDF alone (0.02 Watts/m^2) in the

mentioned cooling cycle.

- A prototype magnetocaloric device was developed that allows for a voltage to be

  produced by the material as it underwent the phase transformation.

- The power output of the device was 1.1 mWatts, which was 213,000 times more

  power than a device without the magnetocaloric material (5.1 nWatts).

6.1. Potential Applications

This research has significant impacts on energy and the environment. The

composite and devices can be potentially used as energy harvesters, thermal switches,

and thermal monitoring systems. The composite materials have the ability to generate a

significant amount of power when actuated through the thermal expansion of the

magnetocaloric material. These materials could be used in situations where there are

cyclic thermo magnetic variations. The composite materials could use these variations in

the temperature and magnetic field to power auxiliary devices. The power generated

could be used for lighting, displaying, or monitoring systems that would supplement the

function of devices.

The composite and laminated devices also have the ability to serve as a thermal

switch or cyclic monitoring system. With the addition of monitoring electronics these

devices could use the voltage produced from these systems to trigger other systems. For

example, in a magnetic refrigerator these systems could serve to count the number of

cycles and monitor the lifetime of refrigerants. Additionally, they could serve to trigger warning signals if the temperature drops below a certain point as a thermal switch. The laminated device offers the advantage in this application that it can be attached directly to the refrigerant in magnetocaloric cooling systems and monitors the cycles of the refrigerant itself.

6.2.   Future Recommendations

The properties of composites and power generation of devices can be further optimized by studying concentration and particle sizes. The laminated device could be improved for power efficiency with the optimal contact areas.

Arc melting process can be improved by removing oxygen and controlling the cooling rate. This would increase the uniformity and reduce the impurity resulting high quality magnetocaloric materials and their devices.

REFERENCES

[1] K. Kelly, TED **TED2005** (2006).

[2] P. S. Peercy, Nature **406,** 1023-1026 (2000).

[3] C. R. Farrar, S. W. Doebling, and D. A. Nix, Philosophical Transactions of the Royal Society of London Series a-Mathematical Physical and Engineering Sciences **359,** 131-149 (2001).

[4] Y. Ammar and S. Basrour, DTIP 2006: Symposium on Design,Test, Integration and Packaging of MEMS/MOEMS 2006**,** 344-348 (2006).

[5] G. K. Ottman, H. F. Hofmann, A. C. Bhatt, and G. A. Lesieutre, IEEE Transactions on Power Electronics **17,** 669-676 (2002).

[6] Y. Qi, N. T. Jafferis, K. Lyons, C. M. Lee, H. Ahmad, and M. C. McAlpine, Nano Letters **10,** 524-528.

[7] T. C. Harman, P. J. Taylor, M. P. Walsh, and B. E. LaForge, Science **297,** 2229-2232 (2002).

[8] S. D. Obertelli, J. R. Cooper, and J. L. Tallon, Physical Review B **46,** 14928-14931 (1992).

[9] B. C. Sales, D. Mandrus, and R. K. Williams, Science **272,** 1325-1328 (1996).

[10] I. Terasaki, Y. Sasago, and K. Uchinokura, Physical Review B **56,** 12685-12687 (1997).

[11] R. Venkatasubramanian, E. Siivola, T. Colpitts, and B. O'Quinn, Nature **413,** 597-602 (2001).

[12] S. R. Anton and H. A. Sodano, Smart Materials & Structures **16,** R1-R21 (2007).

[13] G. W. Taylor, J. R. Burns, S. M. Kammann, W. B. Powers, and T. R. Welsh, IEEE Journal of Oceanic Engineering **26,** 539-547 (2001).

14   C. E. Chang, V. H. Tran, J. B. Wang, Y. K. Fuh, and L. W. Lin, Nano Letters **10,** 726-731.

15   A. Jindal, M. Krishnamurthy, B. Fahimi, and IEEE, 2006 International Symposium on Power Electronics, Electrical Drives, Automation and Motion, Vols 1-3**,** 358-363 (2006).

16   Y. Qin, X. D. Wang, and Z. L. Wang, Nature **451,** 809-U5 (2008).

17   K. Wang, H. Lee, R. Cooper, and H. Liang, Applied Physics a-Materials Science & Processing **95,** 435-441 (2009).

18   Afton Plastics, *PVDF Material Properties Data Sheet* (2010).

19   W. F. Giauque and D. P. MacDougall, Physical Review **43,** 768 (1933).

20   V. K. Pecharsky and K. A. Gschneidner, Physical Review Letters **78,** 4494-4497 (1997).

21   V. K. Pecharsky and K. A. Gschneider, Journal of Alloys and Compounds **260,** 98-106 (1997).

22   S. Aksoy, A. Yucel, Y. Elerman, T. Krenke, M. Acet, X. Moya, and L. Manosa, Journal of Alloys and Compounds **460,** 94-98 (2008).

23   V. K. Pecharsky, G. D. Samolyuk, V. P. Antropov, A. O. Pecharsky, and K. A. Gschneidner, Journal of Solid State Chemistry **171,** 57-68 (2003).

24   V. Basso, M. Lobue, C. P. Sasso, and G. Bertotti, Journal of Applied Physics **99,** 3 (2006).

25   Y. Mudryk, D. Paudyal, V. K. Pecharsky, and K. A. Gschneidner, Physical Review B **77,** 12 (2008).

26   F. Bondino, A. Brinkman, M. Zangrando, F. Carbone, D. van der Marel, D. L. Schlagel, T. A. Lograsso, K. A. Gschneidner, V. K. Pecharsky, and F. Parmigiani, Journal of Physics-Condensed Matter **19** (2007).

27   M. Han, J. A. Paulsen, J. E. Snyder, D. C. Jiles, T. A. Lograsso, and D. L. Schlagel, IEEE, 3252-3254 (2002).

28   M. Han, D. C. Jiles, J. E. Snyder, C. C. H. Lo, J. S. Leib, J. A. Paulsen, and A. O. Pecharsky, Journal of Applied Physics **93,** 8486-8488 (2003).

29   M. Han, D. C. Jiles, J. E. Snyder, T. A. Lograsso, and D. L. Schlagel, Journal of Applied Physics **95,** 6945-6947 (2004).

30   P. J. M. B. Markoli, B. PodMiljšak, I. Škulj, S. Kobe RMZ – Materials and Geoenvironment **56,** 1-8 (2009).

31   H. L. Chen, Y. Du, and C. Y. He, Journal of Alloys and Compounds **462,** 181-186 (2008).

32   W. Choe, V. K. Pecharsky, A. O. Pecharsky, K. A. Gschneidner, V. G. Young, and G. J. Miller, Physical Review Letters **84,** 4617-4620 (2000).

33   B. N. Harmon and V. N. Antonov, Journal of Applied Physics **93,** 4678-4685 (2003).

34   D. S. Kanibolotsky, N. V. Golovataya, O. A. Bieloborodova, and V. V. Lisnyak, Journal of Chemical Thermodynamics **37,** 449-457 (2005).

35   K. Wang, D. Huitink, and M. Cleveland, Texas A&M University, College Station, 2009.

36   D. M. R. Kumar, M. M. Raja, R. Gopalan, R. Balamuralikrishnan, A. K. Singh, and V. Chandrasekaran, Journal of Alloys and Compounds **461,** 14-20 (2008).

37   T. A. Lograsso, D. L. Schlagel, and A. O. Pecharsky, Journal of Alloys and Compounds **393,** 141-146 (2005).

38   Y. Mozharivskyj, A. O. Pecharsky, V. K. Pecharsky, and G. J. Miller, Journal of the American Chemical Society **127,** 317-324 (2005).

39   M. Nazih, A. de Visser, L. Zhang, O. Tegus, and E. Bruck, Solid State Communications **126,** 255-259 (2003).

[40] A. O. Pecharsky, D. A. Gschneidner, V. K. Pecharsky, and C. E. Schindler, Journal of Alloys and Compounds **338,** 126-135 (2002).

[41] A. O. Pecharsky, K. A. Gschneidner, and V. K. Pecharsky, Journal of Applied Physics **93,** 4722-4728 (2003).

[42] V. K. Pecharsky, A. P. Holm, K. A. Gschneidner, and R. Rink, Physical Review Letters **91,** 197204 (2003).

[43] B. Podmiljsak, I. Skulj, B. Markoli, K. Z. Rozman, P. J. McGuiness, and S. Kobe, Journal of Magnetism and Magnetic Materials **321,** 300-304 (2009).

[44] P. V. Trevizoli, C. S. Alves, M. A. B. Mendes, A. M. G. Carvalho, and S. Gama, Journal of Magnetism and Magnetic Materials **320,** 1582-1585 (2008).

[45] O. Ugurlu, L. S. Chumbley, D. L. Schlagel, and T. A. Lograsso, Acta Materialia **54,** 1211-1219 (2006).

[46] W. Wu, A. O. Tsokol, K. A. Gschneidner, and J. A. Sampaio, Journal of Alloys and Compounds **403,** 118-123 (2005).

[47] T. B. Zhang, Y. G. Chen, B. H. Teng, Y. B. Tang, H. Fu, and M. J. Tu, Materials Letters **61,** 440-443 (2007).

[48] W. Dagula, O. Tegus, X. W. Li, L. Song, E. Bruck, D. T. C. Thanh, F. R. de Boer, and K. H. J. Buschow, Journal of Applied Physics **99** (2006).

[49] O. Tegus, E. Bruck, X. W. Li, L. Zhang, W. Dagula, F. R. de Boer, and K. H. J. Buschow, Journal of Magnetism and Magnetic Materials **272,** 2389-2390 (2004).

[50] X. B. Liu, Z. Altounian, and G. H. Tu, Journal of Physics-Condensed Matter **16,** 8043-8051 (2004).

[51] A. Yan, K. H. Muller, and O. Gutfleisch, Journal of Alloys and Compounds **450,** 18-21 (2008).

[52] H. Wada and Y. Tanabe, Applied Physics Letters **79,** 3302-3304 (2001).

53   K. A. Gschneidner, V. K. Pecharsky, A. O. Pecharsky, and C. B. Zimm, *Rare Earths '98*; *Vol. 315-3*, edited by R. C. Woodward (1999), p. 69-76.

54   A. Fujita, S. Fujieda, Y. Hasegawa, and K. Fukamichi, Physical Review B **67** (2003).

55   B. Barkley, Thesis, Texas A&M University, 2010.

56   K. A. Gschneidner and V. K. Pecharsky, International Journal of Refrigeration-Revue Internationale Du Froid **31,** 945-961 (2008).

57   C. Zimm, A. Jastrab, A. Sternberg, V. Pecharsky, K. Gschneidner, M. Osborne, and I. Anderson, *Advances in Cryogenic Engineering, Vol 43 Pts a and B*; *Vol. 43*, edited by P. Kittel (1998), p. 1759-1766.

58   X. Bohigas, E. Molins, A. Roig, J. Tejada, and X. X. Zhang, IEEE Transactions on Magnetics **36,** 538-544 (2000).

59   P. E. Blumenfeld, F. C. Prenger, A. Sternberg, and C. Zimm, Advances in Cryogenic Engineering, Vol 47, Pts a and B **613,** 1019-1026 (2002).

60   J. Z. He, J. C. Chen, and C. H. Wu, Journal of Energy Resources Technology-Transactions of the Asme **125,** 318-324 (2003).

61   D. W. Lu, H. B. Wu, G. Q. Yuan, Y. S. Han, X. N. Xu, and X. Jin, Icec 20: Proceedings of the Twentieth International Cryogenic Engineering Conference**,** 181-184 (2005).

62   V. K. Pecharsky and K. A. Gschneidner, International Journal of Refrigeration-Revue Internationale Du Froid **29,** 1239-1249 (2006).

63   M. Eguchi, Philosophical Magazine **49,** 178-192 (1925).

64   E. Fukada, Ieee Transactions on Ultrasonics Ferroelectrics and Frequency Control **47,** 1277-1290 (2000).

65   M. Tamura, Oqasawar.K, N. Ono, and S. Hagiwara, Journal of Applied Physics **45,** 3768-3771 (1974).

[66] T. Furukawa, M. Date, and E. Fukada, Journal of Applied Physics **51,** 1135-1141 (1980).

[67] S. Miyata, M. Yoshikawa, S. Tasaka, and M. Ko, Polymer Journal **12,** 857-860 (1980).

[68] H. Ohigashi, K. Omote, and T. Gomyo, Applied Physics Letters **66,** 3281-3283 (1995).

[69] J. S. O. Harrison, Z., ICASE-2001-43 **NAS 1.26:211422** (2001).

[70] T. Jee, Thesis, Texas A&M Univeristy, 2005.

[71] H. E. T. Swanson, E., National Bureau of Standards **539,** 95 (1953).

[72] T. F. Ben Tupper, Gilles Carpentier, 1.43 ed. (NIH, 2009).

VITA

Michael Allen Cleveland

EDUCATION

2008-2010	*Masters of Science*, Texas A&M University, College Station, TX
	Major in Mechanical Engineering with an Emphasis in Materials
2005-2008	*Bachelor of Arts*, Austin College, Sherman, TX
	Major in Physics, Minor in Mathematics

ADDRESS

Texas A&M University
Mail Stop 3123
College Station, Texas 77843
Michaelc8264@gmail.com

PROJECT EXPERIENCE

Fall 2008 – Present - Development of Hybrid Insect Systems, Dr. Hong Liang
Texas A&M University
Studied insect locomotion and performance for bio-inspired robotics applications.

Fall 2008 – Present - Applications and Characterization of $Gd_5Si_2Ge_2$, Dr. Hong Liang
Texas A&M University
Designed, characterized and evaluated a variety of methods for monitoring $Gd_5Si_2Ge_2$ for use in magneto-caloric refrigerators
Built a robust thermal switch for use in situations where thin film sensors are ideal by making PVDF/ $Gd_5Si_2Ge_2$ composites
Studied the effects of oxygen impurities on the micro-structural phase behavior of as-cast $Gd_5Si_2Ge_2$

Summer 2007 - *Optoelectronic Properties of ZnO Nanorods*, Dr. Yuri Strzhemechny
Texas Christian University
Designed and carried out optical experiments pertaining to material properties of the lattice structure of ZnO nano-crystals. Presented results at the Texas Section meeting of the American Physical Society in October 2007

Spring 2007 - *Improvement of a Cryogenic Measuring System*, Dr. Andra Troncalli
Austin College
Eliminated problems in the electrical and vacuum systems of a cryostat used to study high temperature superconductors